

12-15-2018

Fluid Structure Interaction Study of the Obstructive Sleep Apnea and Surgical Treatment Using Suture-Patch Device on the Patient's Tongue

Yang Liu

Follow this and additional works at: <https://digitalscholarship.unlv.edu/thesesdissertations>



Part of the [Mechanical Engineering Commons](#)

Repository Citation

Liu, Yang, "Fluid Structure Interaction Study of the Obstructive Sleep Apnea and Surgical Treatment Using Suture-Patch Device on the Patient's Tongue" (2018). *UNLV Theses, Dissertations, Professional Papers, and Capstones*. 3503.

<http://dx.doi.org/10.34917/14279650>

This Dissertation is protected by copyright and/or related rights. It has been brought to you by Digital Scholarship@UNLV with permission from the rights-holder(s). You are free to use this Dissertation in any way that is permitted by the copyright and related rights legislation that applies to your use. For other uses you need to obtain permission from the rights-holder(s) directly, unless additional rights are indicated by a Creative Commons license in the record and/or on the work itself.

This Dissertation has been accepted for inclusion in UNLV Theses, Dissertations, Professional Papers, and Capstones by an authorized administrator of Digital Scholarship@UNLV. For more information, please contact digitalscholarship@unlv.edu.

FLUID STRUCTURE INTERACTION STUDY OF THE OBSTRUCTIVE SLEEP APNEA
AND SURGICAL TREATMENT USING SUTURE-PATCH DEVICE
ON THE PATIENT'S TONGUE

By

Yang Liu

Bachelor of Sciences– Electrical Engineering
Harbin Institute of Technology
2007

Master of Sciences – Mechanical Engineering
University of Nevada, Las Vegas
2011

A dissertation submitted in partial fulfillment
of the requirements for the

Doctor of Philosophy – Mechanical Engineering

Department of Mechanical Engineering
Howard R. Hughes College of Engineering
The Graduate College

University of Nevada, Las Vegas
December 2018

Copyright by Yang Liu, 2018

All Rights Reserved

November 9, 2018

This dissertation prepared by

Yang Liu

entitled

Fluid Structure Interaction Study of the Obstructive Sleep Apnea and Surgical Treatment
Using Suture-Patch Device on the Patient's Tongue

is approved in partial fulfillment of the requirements for the degree of

Doctor of Philosophy – Mechanical Engineering
Department of Mechanical Engineering

Yi-Tung Chen, Ph.D.
Examination Committee Chair

Kathryn Hausbeck Korgan, Ph.D.
Graduate College Interim Dean

Woosoon Yim, Ph.D.
Examination Committee Co-Chair

Robert F. Boehm, Ph.D.
Examination Committee Member

Mohamed B. Trabia, Ph.D.
Examination Committee Member

Zhonghai Ding, Ph.D.
Graduate College Faculty Representative

ABSTRACT

FLUID STRUCTURE INTERACTION STUDY OF THE OBSTRUCTIVE SLEEP APNEA AND SURGICAL TREATMENT USING SUTURE-PATCH DEVICE ON THE PATIENT'S TONGUE

by

Yang Liu

Dr. Yi-Tung Chen, Examination Committee Chair
Professor, Department of Mechanical Engineering
University of Nevada, Las Vegas

Up to 14% of the U.S. population is estimated to have obstructive sleep apnea (OSA) related to obesity, and there is increased incidence occurring worldwide. While treatment with continuous positive airway pressure (CPAP) resolves airway obstruction, patient compliance is relatively low. Alternative interventions are available to treat OSA patients; however, their outcomes have had variable results. For example, current technologies have demonstrated an inability to define and treat the specific anatomical site(s) causing the obstruction, resulting in suboptimal modifications of the airway and poor control of OSA.

In the current study, a three-dimensional (3-D) fluid-structure interaction (FSI) numerical simulation has been applied to simulate upper airway (UA) collapse, without considering the individual muscles. The objective of this study is to demonstrate how to use the two-way FSI numerical simulation to study the characteristics of and identify the precise location of an upper airway collapse on female and male patients with OSA. This task was accomplished using

Simpleware[®], which is medical image processing software, and ANSYS[®] Fluent, which is computational fluid dynamics (CFD) and structural software. Simpleware[®] is able to process a patient's 3-D computed tomography (CT) scan image and render this airway image to ANSYS[®] Fluent in order to generate the computational domains of fluid and structure. During FSI numerical simulation, areas that are prone to collapse and precipitate apneic episodes were identified at the tip of the soft palate and the base of the tongue, with intrathoracic pressures as low as -1370 Pa. These results are consistent with anatomical structures that are currently indicated and targeted in the treatment of OSA. The negative pressure is similar to previous values reported in human esophageal pressure measurements in UA resistance syndrome. This improved two-way FSI numerical simulation, which is the first to accurately model the UA geometry in OSA, can allow virtual modification of the airway before actual clinical treatment by ear, nose, and throat (ENT) medical doctors.

The improved two-way FSI numerical simulation was later used to model and simulate a unique suture-patch device, which can be used to virtually apply force to the tongue. Based on the numerical simulation results, this device can effectively reduce the risk of UA occlusion and open up the UA at the pharynx 92% of its original area under the peak inhale volume for a specific patient. This provides a possible treatment for the patient, instead of conducting tissue removal or requiring use of a CPAP mask. Three locations to put the suture-patch device on the patient's tongue were compared in the study, and the suture-patch at location 2 is recommended. Next, the bisection method is used to find the minimum force needed to open up the airway from occlusion. The results show that 1.25 N is the recommended force.

Both male and female OSA patients were studied and compared in three different aspects: geometry, flow field, and tissue movement. The results from this case study show that tissue

movement does not depend only on the apnea and hypopnea index (AHI). They show that classic symptoms, like snoring, should not be the only diagnosis of OSA. Anyone with restless sleep or daytime fatigue, with snoring syndrome, should visit an ENT doctor and have a clinical sleep test in order to find out whether he or she has OSA.

Using the current FSI development, a patient-specific numerical simulation can be carried out prior to surgery to virtually audit different treatments, when the patient is diagnosed with severe OSA and needs surgical treatment. Then the ENT doctor can discuss the best treatment with the patient based on the simulation results. Moreover, ENT doctors and patients will be able to visualize the outcome of virtual surgery from numerical simulations. This will give patients more confidence and help to alleviate their trepidation about treatment options. Moreover, the patient-specific numerical simulations can be used to compare different OSA cases to study the characteristics they have in common. Therefore, patients can understand more about OSA, and ENT doctors can determine the possible ways to conduct the best treatment in the near future.

ACKNOWLEDGEMENTS

Working as a Ph.D. student is a magnificent dream as well as a challenging experience to me. During all these years, many people have granted me useful help in shaping up my academic career. It was hardly possible for me to thrive in my doctoral work without the precious support of these mentors, friends, and families. Here is a small tribute to these people.

First of all, I wish to express my deepest thanks to my supervisor Dr. Yitung Chen for introducing me to this biomechanical research topic. It is a challenging topic that crosses over fluid dynamics, solid mechanics, and medical anatomy and physiology. Thanks to his consistent guidance, encouragement, patience, and valuable suggestions, as well as allowing me extra time, so that I can finally finish my project. I am extremely fortunate to have him as my advisor for my doctoral research.

I am also thankful to my co-advisor Dr. Woosoon Yim. He has helped and guided me in the experimental work during my Ph.D. study. I would also like to thank my committee members of Dr. Robert Boehm, Dr. Mohamed Trabia, and Dr. Zhonghai Ding, who have provided me many valuable suggestions during the course of the study. Thanks to Dr. Jennifer Mitchell for her help during the porcine tissue experiments and measurements, and Dr. Robert Wang for his guidance in the medical field of OSA. I would like to thank my parents for their endless encouragement and supports. I want to dedicate this dissertation to my dear mother, who came over to the U.S. to stay with me in the most difficult time and help me to finish my Ph.D. work in the final stage.

TABLE OF CONTENTS

ABSTRACT.....	iii
ACKNOWLEDGEMENTS.....	vi
TABLE OF CONTENTS.....	vii
LIST OF TABLES.....	xi
LIST OF FIGURES.....	xii
NOMENCLATURES.....	xv
CHAPTER 1 INTRODUCTION TO OBSTRUCTIVE SLEEP APNEA.....	1
1.1 Overview and Background.....	1
1.2 Airway Anatomy.....	2
1.3 Causes of Obstructive Sleep Apnea.....	6
1.4 Current Clinical Treatments.....	6
1.5 Health Effects.....	10
1.6 Airway Collapse Pressure.....	11
1.7 Literature about Numerical Simulations.....	11
CHAPTER 2 MEDICAL IMAGE PROCESSING.....	14
2.1 3-D Geometry Built Up.....	14
2.2 Segmentation of Airway Tissues and Bones.....	15
CHAPTER 3 ELASTICITY EXPERIMENTS.....	20

3.1 Specimen Preparation.....	20
3.2 Mechanical Apparatus.....	20
3.3 DMA and the Viscoelastic Voigt Model.....	22
3.4 Validation of Constrained Method against Previous Studies.....	24
3.5 Specially Designed Testing for the Epiglottis.....	28
3.6 Results and Discussions	29
3.6.1 Tissue test in lateral and axial directions.....	29
3.6.2 The constrained Young’s modulus vs. frequency	30
3.6.3 The Young’s modulus calculated from the constrained measurements	31
3.6.4 The advantage and limitation of constrained experiments	33
3.6.5 Precondition.....	33
3.6.6 Reasons for the difference compared to the published data	34
3.6.7 Future use of the constrained method.....	34
3.6.8 Viscoelasticity vs. linear elasticity	35
CHAPTER 4 FLUID-STRUCTURE INTERACTION NUMERICAL MODELING.....	37
4.1 Coupled System and Governing Equations.....	37
4.2 Boundary Conditions.....	39
4.3 Solver Settings.....	41
4.4 Mesh Independence Study	42
CHAPTER 5 STUDY OF UPPER AIRWAY COLLAPSE.....	44

5.1 Investigation of Velocity Field in the Pharynx	44
5.2 Investigation of Wall Shear Stress	45
5.3 Investigation of Pressure Field in the Pharynx	46
5.4 Investigation of Wall Displacement.....	49
5.5 Conclusion.....	51
CHAPTER 6 ASSESSMENT OF POSSIBLE TREATMENTS: SUTURE-PATCH DEVICE ..	53
6.1 Description of the Device and Material Selection	53
6.2 Velocity Streamlines with and without Force	55
6.3 The Study of Upper Airway Collapse	57
6.4 The Patch Position Study	59
6.5 The von-Mises Stress	60
6.6 The Minimum Force Required.....	61
6.7 Conclusion.....	66
CHAPTER 7 COMPARISON OF A MALE AND A FEMALE PATIENT.....	67
7.1 Geometry Difference between the Male and the Female Patient.....	67
7.2 Boundary Conditions and Solver Settings	68
7.3 Investigation of the Flow Field and Tissue Movement.....	69
7.3.1 Comparison of the fluid flow field	69
7.3.2 Comparison of the soft palate movement.....	73
7.4 Conclusion.....	75

CHAPTER 8 CONCLUSIONS AND FUTURE WORKS.....	77
8.1 Conclusions.....	77
8.2 Future Research.....	78
REFERENCES	80
CURRICULUM VITAE.....	90

LIST OF TABLES

Table 1. Comparison with the Young's modulus from other researchers. 27

Table 2. The Young's modulus of the middle of the tongue from the unconstrained experiment.
..... 29

Table 3. The Young's modulus calculated from the constrained measurements (@ 1 Hz, 3 mm).
..... 31

LIST OF FIGURES

Figure 1. Pharyngeal airway in human body [6].....	3
Figure 2. Sub-regions of the pharyngeal airway [7].	4
Figure 3. Muscles of the pharynx [8].....	5
Figure 4. CPAP therapy: the mask and the air flow [11].....	7
Figure 5. Mandibular advance device oral appliance therapy [16].....	8
Figure 6. TRM tongue appliance [17].....	9
Figure 7. Before and after UPPP surgery [19].....	10
Figure 8. 3-D CT images of patients A and B.	15
Figure 9. Respiratory tract-the fluid domain for patients A and B.	16
Figure 10. 2-D segmentation of the geometries for patients A and B.	18
Figure 11. 3-D segmentation of the geometries for patients A and B.	18
Figure 12. (a) Schematic of the DMA 8000 analytic train; (b) DMA 8000 analytic train [48]....	21
Figure 13. Porcine head fixation and metal rod connection.	21
Figure 14. Porcine head and metal wire connection.	22
Figure 15. Viscoelastic Voigt model of the tissue.	24
Figure 16. Unconstrained measurements: porcine tongue tissue being held between plastic clamps.	25
Figure 17. Constrained measurements: porcine tongue tissue intact with the lower jaw.	26
Figure 18. Unconstrained measurements: epiglottis cartilage.	28
Figure 19. Comparison of the constrained Young's modulus at different requested frequencies.	31
Figure 20. Load-displacement curve of the epiglottis at the tested frequency of 1 Hz.	36
Figure 21. Meshed fluid geometry based on patient A.	43

Figure 22. Comparison of (a) velocity and (b) pressure distribution along the typical line computed using different mesh resolutions based on patient A.	43
Figure 23. Velocity streamlines in the upper airway at different times (a) 0.1 s, (b) 0.2 s, (c) 0.3 s, (d) 0.35s based on patient A.	45
Figure 24. Wall shear stress along the anterior polyline (intersection of the sagittal plane and the FSI interface) based on patient A.....	46
Figure 25. Pressure contour of the horizontal planes of the upper airway at time (a) 0.1 s, (b) 0.2 s, (c) 0.3 s, (d) 0.35s based on patient A.	48
Figure 26. Prediction of (a) the first point touching and (b) full closure of the upper airway based on patient A.....	48
Figure 27. Deformation at four locations: the tip of the soft palate, base of the tongue, tip of the epiglottis, and hyoid bone based on patient A.	50
Figure 28. Deformation and stress vs. time at the tip of the soft palate based on patient A.....	51
Figure 29. The suture-patch locations in the tongue on patient B.	54
Figure 30. Velocity streamlines of the UA with (a) no force; (b) 5 N force based on patient B..	56
Figure 31. Cross-sectional plane showing the location of collapse based on patient B.	57
Figure 32. The area change due to the location of the patch based on patient B.....	58
Figure 33. The deformation contour with 5 N force applied along the suture at the three patch locations based on patient B.	59
Figure 34. The von-Mises stress on the suture and in the tissue with 5 N force applied along the suture at the three patch locations based on patient B.	60
Figure 35. Top view of the cross-sectional deformation contour of plane 4 as (a) 2.5 N (b) 1.25 N (c) 0.63 N (d) 0.94 N force applied along the suture.	63

Figure 36. The cross-sectional area of plane 4 as 0-5 N forces applied along the suture.	64
Figure 37. The cross-sectional area of plane 4 as 0.63-5 N force applied along the suture compared with the original area in the CT scan.	65
Figure 38. Respiratory- fluid domains of the male (a) and female (b) patient.	68
Figure 39. Pressure contour at different time for the male patient.	70
Figure 40. Pressure contour at different time for the female patient.	71
Figure 41. Area-weighted average of pressure along the upper airway at the peak flow rate	71
Figure 42. Velocity streamlines at different time for the male patient.	72
Figure 43. Velocity streamlines at different time for the female patient.	73
Figure 44. Tip of the soft palate movement at different time for the male patient.	74
Figure 45. Tip of the soft palate movement at different time for the female patient.	75

NOMENCLATURES

a, b, l	Specimen size (mm)
D	Structural displacement (mm)
E	Young's modulus (Pa)
E^*	Dynamic modulus (Pa)
E'	Storage modulus (Pa)
E''	Loss modulus (Pa)
F	Force (N)
k	Turbulence kinetic energy (m^2/s^2)
K^*	Dynamic stiffness (N/m)
K'	Storage stiffness (N/m)
K''	Loss stiffness (N/m)
p	Pressure (Pa)
S	Shape factor
u	Velocity (m/s)
Y_0	Unconstrained Young's modulus (Pa)
Y_b	Constrained Young's modulus (Pa)
$\alpha, \beta, \beta^*, \sigma, \sigma^*$	Closure coefficients in turbulence model
δ	Phase angle (rad)
ε_{ij}	Strain tensor
μ	Dynamic viscosity ($Pa \cdot s$)
ν	Poisson's ratio

ν_T	Kinetic eddy viscosity (m^2/s)
ρ	Density (kg/m^3)
σ_{ij}	Cauchy stress tensor (Pa)
ω	Specific dissipation (1/s)
Ω^F	Fluid domain
Ω^S	Solid domain

CHAPTER 1 INTRODUCTION TO OBSTRUCTIVE SLEEP APNEA

1.1 Overview and Background

Obstructive sleep apnea (OSA), typically defined as a repetitive collapse of the airway causing interruption of airflow for 20 to 40 seconds, is a common sleep disorder affecting twenty million people in the U.S. alone [1]. Patients with OSA awake several times an hour throughout the night and often complain of headaches, chronic fatigue, and difficulty staying awake during the daytime. Additionally, cyclically low blood oxygen levels may result in severe conditions, such as uncontrollable hypertension, stroke, arrhythmias, pulmonary disease, and even death. Although sleep apnea was not named or officially labeled as a syndrome until the twentieth century, the record shows that people noticed the symptoms nearly two hundred years ago. In Charles Dickens' novel of *The Pickwick Papers*, which was published in 1836, "the fat boy" Joe exhibited symptoms that are an accurate clinical picture of an OSA patient [2]. In the early twentieth century, sleep apnea symptoms started to be lumped together by medical doctor Willian Osler, who must have been a reader of *The Pickwick Papers*, named it as the "Pickwickian syndrome."

However, the initial investigations about Pickwickian syndrome only consider body fat as the reason for the symptoms. Although many patients are overweight, later studies have confirmed that obesity is not the only reason. Without a doubt, extra fat around the neck can certainly increase the pressure on the throat muscle tissues when a person lies down; however, it cannot explain why many slender people, even young children, have the OSA syndrome [3].

From the 1950s to 1960s, researchers were aware of the major problem in OSA: the patients are breathing improperly during sleep. Moreover, the researchers have developed a collection of symptoms that may happen together.

Research engaged in determining the reasons, symptoms, and treatments of sleep apnea became popular in the 1970s. In the beginning, researchers observed sleep and breathing in dogs, and used tracheotomies to treat the condition. At that time tracheotomies were also the treatment for humans. Although it sounds scary, it was the only treatment researchers could realize to let air flow through airway into the lungs.

In the early 1980s, Colin Edward Sullivan [4] developed a customized mask for dogs, and later humans, for breathing during sleep. The mask delivers positive pressure airflow, which is an early form of continuous positive airway pressure (CPAP). The developed mask also worked well for five human subjects in an initial study in which Sullivan wanted to promote this kind of treatment. Patients did not accept the mask treatment at that time [5], but over the years, CPAP has become the standard treatment for many sleep apnea sufferers.

1.2 Airway Anatomy

The region of the upper airway (UA) related to OSA ranges from the nasal cavity down to the larynx inlet as shown in Figure 1 [6]. The pharyngeal airway includes four areas: (i) nasopharynx, which is the lower half of the nasal cavity; (ii) velopharynx, which covers the area level with the soft palate; (iii) oropharynx, which is the area level with oral cavity; and (iv) hypopharynx, which includes the area below the tongue to the inlet of the larynx. These areas have been highlighted and labeled in Figure 2 [7].

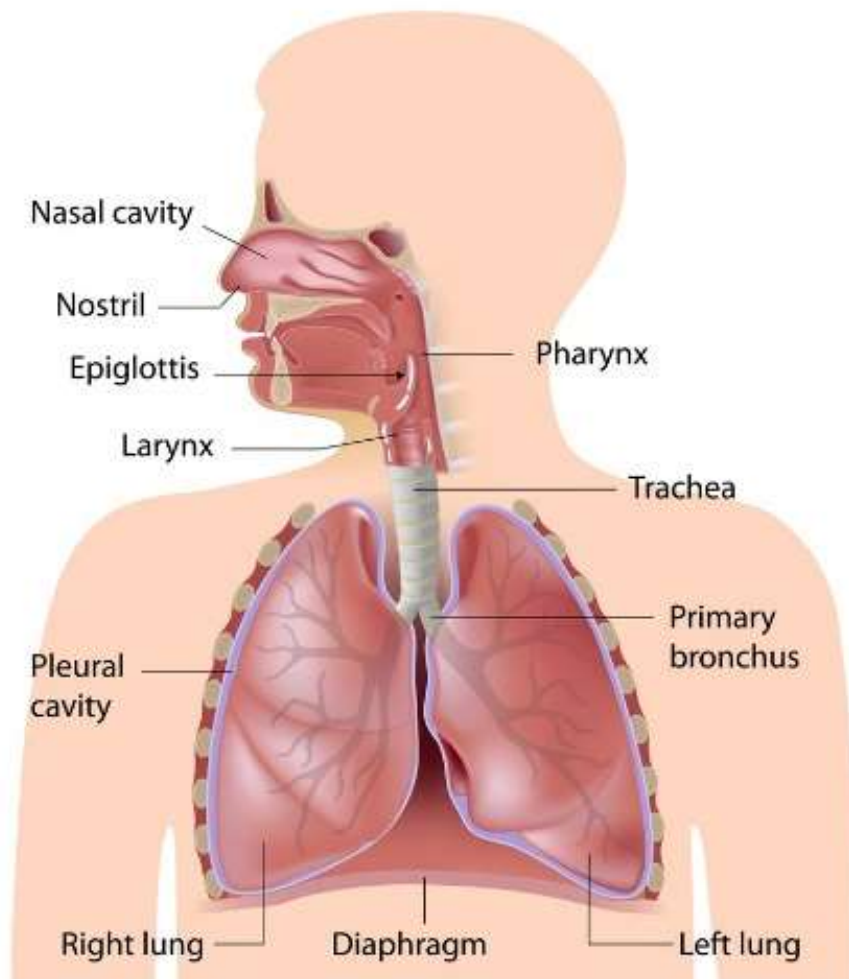


Figure 1. Pharyngeal airway in human body [6].

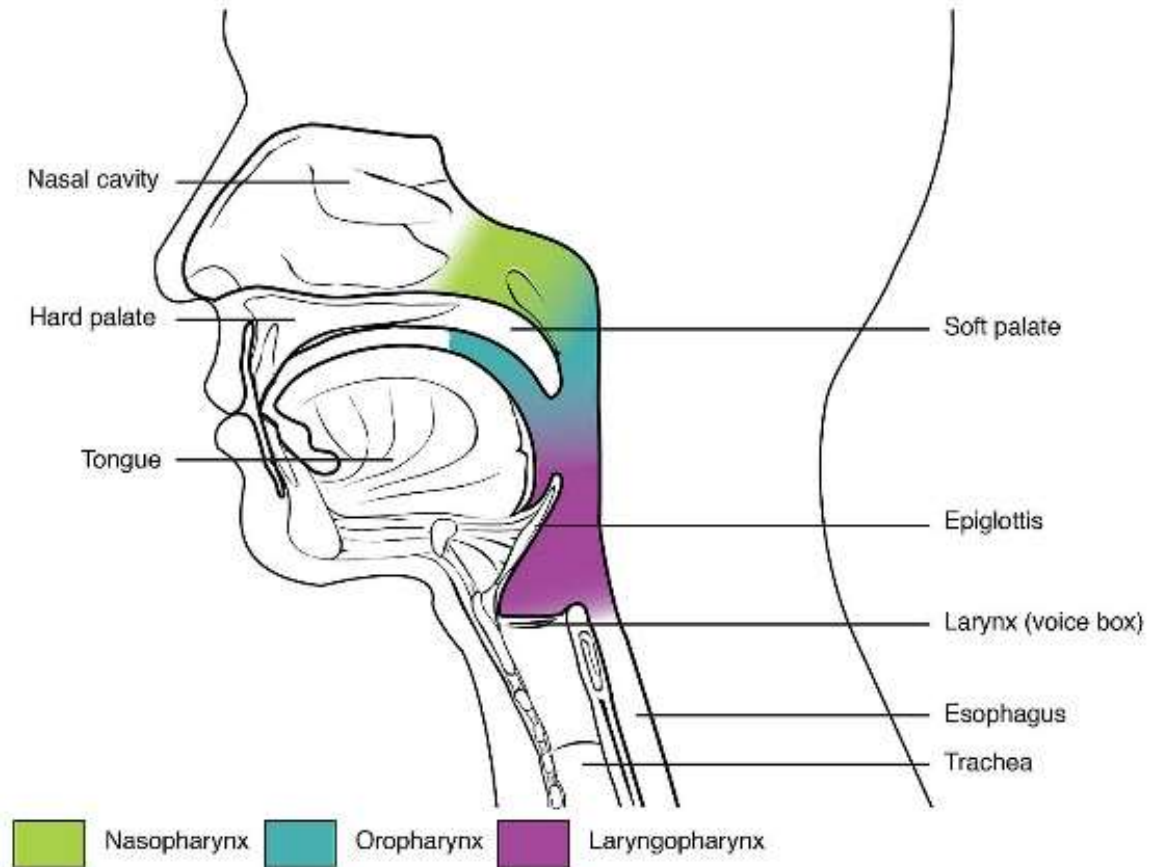


Figure 2. Sub-regions of the pharyngeal airway [7].

The pharynx is the part of the throat that is behind the nose and mouth and above the larynx and esophagus. It is the conducting zone of both the respiratory system and the digestive system. It is also the area that is most prone to experience airway collapse. The region of pharynx can be divided into three parts from top to bottom, due to the location: nasopharynx, oropharynx, and laryngopharynx, as shown in Figure 2.

The pharyngeal airway wall is formed by four layers of structure: from inside to outside are the mucosa layer, fiber layer, muscular layer, and fascial layer. The muscular layer consists of the outer constrictor muscles and inner longitudinal muscles; each sub-group consists of three

primary muscles each. The constrictor muscle is made up of the superior, middle and inferior constrictors, all of which wrap around the airway, as shown in Figure 3 [8]. These muscles constrict to propel bolus downwards (an involuntary process). The longitudinal muscle subgroup is made up of the stylopharyngeus, salpingopharyngeal, palatopharyngeal, which are also shown in Figure 3. These muscles descend from origins near the base of the skull and connect to different parts of the pharyngeal wall, and their main function is to elevate the pharyngeal wall while swallowing.

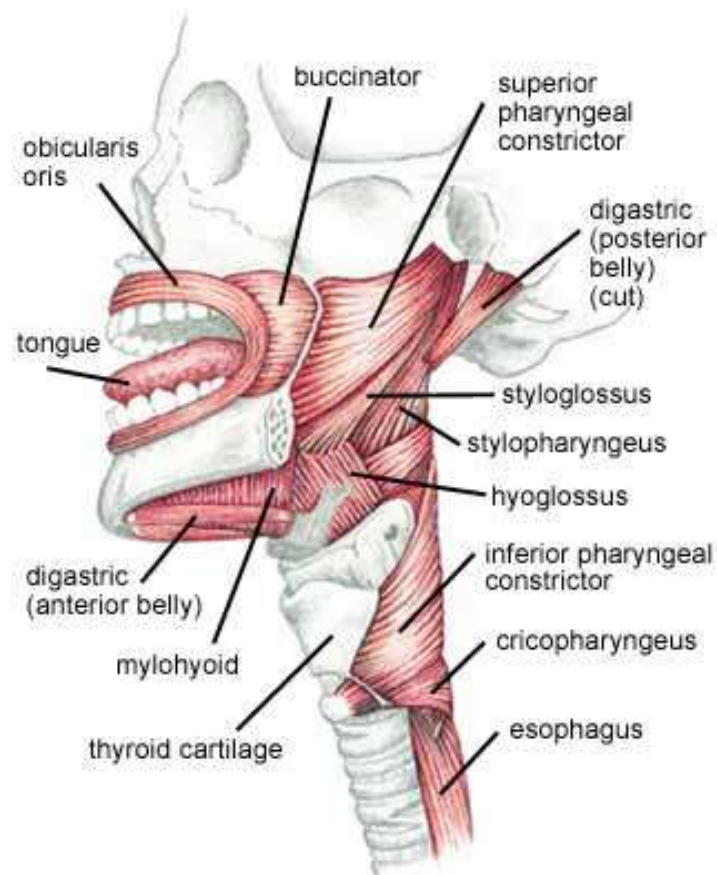


Figure 3. Muscles of the pharynx [8].

1.3 Causes of Obstructive Sleep Apnea

Most cases of OSA in adults are believed to be initiated by being overweight or obese, which cause extra soft tissues in the mouth and throat. When the muscles are relaxed during sleep, these soft tissues may cause the airway to suffocate. Increased soft tissue due to obesity around the airway brings on a narrowed airway. Others believe the reason of OSA is the loose neurological stiffness of the tongue tissue, which may be caused by old age (natural or premature), brain injury (permanent or temporary), or drugs and alcohol. The geometry of the UA varies from person to person, and it may also determine the breathing status. Moreover, sleeping habits (head up or head down, sleeping on the side or the back) are also crucial to apnea characteristics.

In children's OSA cases, the cause often includes enlarged tonsils or adenoids. Sometimes dental problems, like overbite, will also cause OSA. Studies have shown that bottle-feeding and pacifiers promote the formation of a hard palate and narrow arch, characteristics that may cause sleep apnea in children [9].

1.4 Current Clinical Treatments

The CPAP device is the most common way of treatment for OSA patients to use during their sleep. This therapy involves breathing the ambient air pressurized between 5 and 30 cmH₂O through either a nasal or full-face mask [10], as shown in Figure 4. By breathing the pressurized air, the static pressure within the airway during inhalation increases, and then resists the UA collapse. The pressure can be adjusted to match the collapsibility of the individual patient's airway. Although the pressurized air is heated and humidified, breathing the pressurized air may cause airway dry up syndrome, which is uncomfortable for most patients. The masks used for

CPAP applications usually have holes in them that allow an outflow of exhaled air to escape from the mask [11].

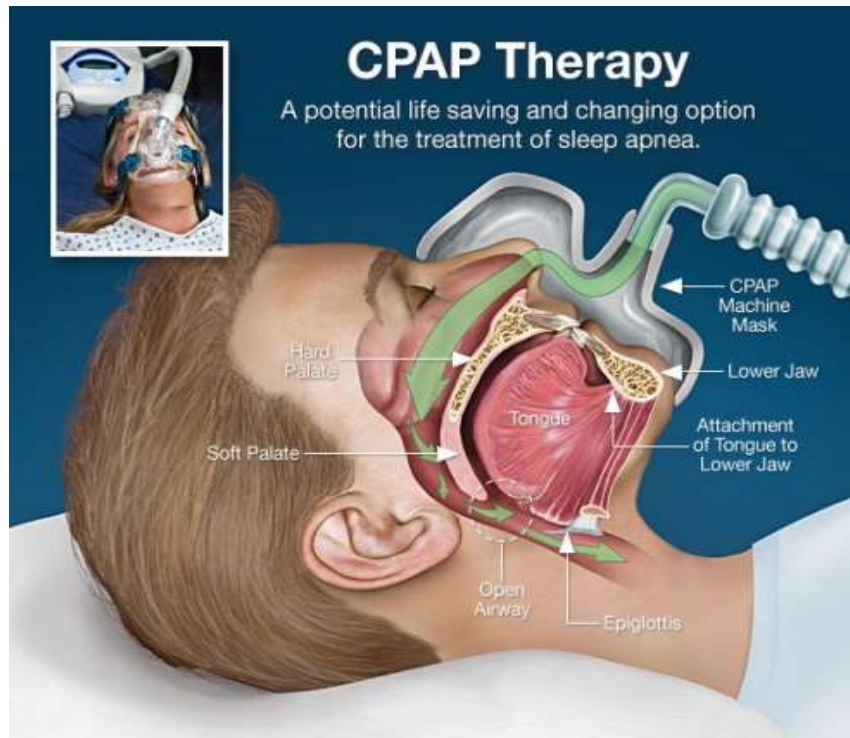


Figure 4. CPAP therapy: the mask and the air flow [11].

While the CPAP devices are effective in preventing apneas in patients who suffer from OSA [12, 13], they are not very comfortable for many patients to wear, especially when those patients are trying to fall into sleep. The process of breathing the pressurized air is also uncomfortable. It can result in side effects such as a dry or crusty nose, even though the pressurized air is heated and humidified. Therefore, while the use of CPAP devices is effective in preventing apneas, the resulting side effects make them unusable for many patients [14].

Oral appliances are used to advance the jaw or hold the patient's mouth open while they sleep. Treatment of OSA by oral appliances is not as effective as CPAP and tends only to be used in mild cases of OSA. However, it does improve symptoms [15]. An oral appliance like mandibular advancement device (MAD), as shown in Figure 5 [16], works by pushing the lower jaw and tongue slightly forward. Most MADs are adjustable, allowing dentists to adjust the position of the lower jaw for maximum effectiveness. Similarly, a tongue retaining mouthpiece (TRM), as shown in Figure 6 [17], is held by the teeth, but it has a small compartment that sucks the tongue forward to prevent it from collapsing back into the airway. The advantages of using oral appliances are that they are more user-friendly, have less harmful side effects, and cost less to set up [18]. The disadvantages are that they may cause jaw pain or damage, and may cause loosening of dental restorations.



Figure 5. Mandibular advance device oral appliance therapy [16].



Figure 6. TRM tongue appliance [17].

Also available are tissue removal treatments, such as tonsillectomy, adenoidectomy, and uvulopalatopharyngoplasty (UPPP) to help patients and prevent OSA, as shown in Figure 7 [19]. Surgical treatments involve the partial removal of the tonsil, adenoid, or soft palate tissue, while the airway walls at the oropharynx level are reshaped; the walls of the oropharynx are tethered in the lateral direction to open the oropharyngeal section of the airway. Surgical treatment of OSA by UPPP, of which the success rate is less than 40%, is not as effective as CPAP [20]. Since the palate is like a valve that separates the nose from the mouth, surgeons should carefully remove the right amount of tissue. It has been suggested that the surgical plan and the procedure selection should be customized for each patient, which may be more effective in preventing obstructions in the oropharynx and velopharynx regions [21].

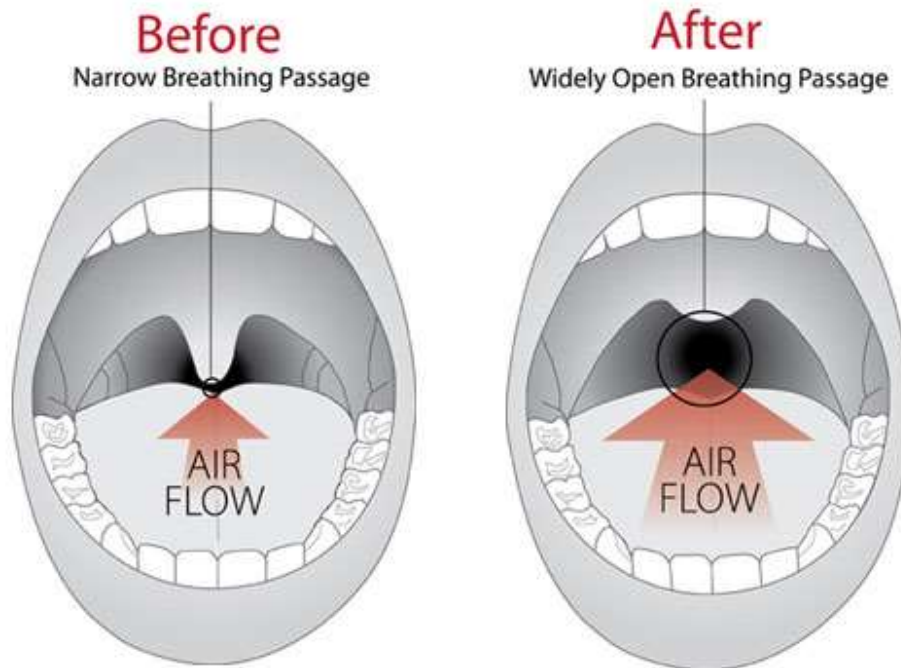


Figure 7. Before and after UPPP surgery [19].

Some other methods to treat OSA have been provided by medical doctors in recent years. The night shift is a device to be worn on the back in the night, which starts to vibrate when the user begins to sleep on the back, and slowly increases the intensity until the user changes sleep positions. The pillar procedure puts three small rods in the soft palate to stiffen it, in its way of discouraging the apnea. The inspired UA stimulation therapy monitors the breathing pattern from the heartbeat and delivers mild stimulation to the hypoglossal nerve, which controls the movement of the tongue to keep the airway open. New inventions have been flourishing continuously in recent years. However, the treatment for a patient with severe OSA still remains a formidable challenge.

1.5 Health Effects

People who suffer from OSA can experience a wide range of symptoms, and the most common is daytime tiredness. It is also shown that OSA increases the likelihood that the patient will suffer from cardiovascular diseases and disorders such as high blood pressure, strokes, coronary artery disease, and cardiac arrhythmias [22]. It has also been proposed that OSA may affect the body's sensitivity to insulin, as well as affecting the patient's memory and ability to concentrate [23].

It has been noted that a person can suffer from OSA even if he or she is not overweight. However, it is commonly accepted that patients who suffer from OSA will on average have a higher body mass index (BMI) and tend to be more obese than healthy people [23]. More specifically, it is shown that OSA patients carry more weight around the neck than weight-matched controls and snorers who do not suffer from OSA [23]. As well as increased obesity in the neck region, a small inset jaw and hyoid bone have also been attributed to causing and increasing the severity of OSA by crowding the area around the airway [23].

1.6 Airway Collapse Pressure

A common variable used in OSA research is the critical pressure (P_{crit}), or the pressure at which the pharyngeal airway collapses. The value of P_{crit} varies from person to person; however, in general, the patient who suffers from OSA has higher P_{crit} in the pharyngeal airway, compared to an age-and-weight-match healthy person [24]. A healthy person, on the other hand, generally has P_{crit} less than 8 cmH₂O [25, 26]. Suratt et al. [27] have demonstrated that the pharyngeal airway of healthy controls will not collapse, while the pharyngeal airway of OSA patients will generally collapse at P_{crit} values between -17 and -52 cmH₂O. This was achieved by subjecting both OSA patients and healthy controls to sub-atmospheric pressures.

1.7 Literature about Numerical Simulations

Recent research employing numerical modeling and simulation of the airway study have led to useful results and promising possibilities for future applications in OSA diagnosis and treatment. Many researchers have used computational fluid dynamics (CFD) to simulate the human UA. In 2009, Wang et al. [28] used CFD to study the respiratory airflow dynamics within a human UA. In the same year, Mylavarapu et al. [29] validated different CFD methodologies used for human UA flow simulations. Several studies then attempted to assess and predict the effect of various treatments [30-33]. Liu et al. [30] found that the wall shear stress oscillating signal can be utilized to quantify breathing quality. Fletcher et al. [31] studied the effect of genioglossal advancement with CFD analysis. Mylavarapu et al. [32] assessed four virtual surgeries in different combinations with the intention of remedying the obstructed airway, using virtual surgery, based on the airway models assessed by comparisons with the pre-treatment flow modeling results. Luo et al. [33] used CFD for evaluation of adenotonsillectomy surgery outcomes in obese children with OSA. Yu et al. [34] compared statistical differences between different apnea-hypopnea index (AHI) groups. Cheng et al. [35] studied ten different cases of pressure distributions along the pre- and postoperative UAs, and the results showed a robust patient-specific uniqueness.

Recent research in OSA has integrated CFD with fluid-structure interaction (FSI), which has successfully provided better results and more in-depth information from simulations. Sun et al. [36] first used FSI for numerical simulation of the soft palate movement and airflow in the nasopharynx. Chouly et al. [37] first used FSI in a simplified manner for the geometry of the airway at the base of the tongue. With a highly simplified geometry, Chouly et al. could reduce the computational time to the order of 10 mins. In 2010, Mylavarapu et al. [38] created a 2-D geometry of the whole UA domain and carried out FSI analysis with different inlet and outlet

pressures. Huang et al. [39] built a 3-D FSI model to explore the movement of the base of the tongue during the breathing cycle. In 2012, Zhu et al. [40] built a 3-D FSI model to study the soft palate movement during respiration. In the same year, Wang et al. [41] used the FSI model for UA study, and found that the resistance of UA decreased considerably after nasal surgery. Zhao et al. [42, 43] developed a novel FSI model to analyze the UA occlusion and flow dynamics in OSA patients. However, the pharyngeal structure was described as a “collapsible homogeneous tube,” which differs from the real physiological structure. Pirnar et al. [44] predicted soft palate flutter during the expiratory period of breathing, and evaluated the flutter frequency by performing 3-D FSI simulations of the human UA. They modeled the soft tissue as homogeneous and isotropic material, and used the linear elasticity assumption for the soft tissue.

All the previous published FSI simulations were highly simplified, and only included the tongue or the soft palate tissue, so the results may not be accurate. In the present study, the 3-D two-way FSI model has been developed using different tissues around the UA, which is more advanced than the previously published studies. The developed two-way FSI model has also been used to study the effect of a suture-patch device, as well as different behavior between two patients. The developed 3-D two-way FSI model can provide a patient-specific simulation, which allows medical doctors to visually find the best treatment for patients.

CHAPTER 2 MEDICAL IMAGE PROCESSING

2.1 3-D Geometry Built Up

The computed tomography (CT) scan images of a 64-year-old female patient (patient A) and a 61-year-old female patient (patient B) diagnosed with OSA by polysomnography were analyzed in the present study. Patient A has a BMI of 35, with an apnea and hypopnea index (AHI) of 87.6/hr. Patient B has a BMI of 36 with an AHI of 80/hr. The AHI shows the number of breathing disturbances (apneas and hypopneas) the patient has per hour, and is the standard indicator of the severity of sleep apnea. An AHI of less than 5 is considered normal; an AHI from 5 to 15 indicates mild OSA; an AHI from 15 to 30 denotes moderate; while an AHI greater than 30 is designated as severe OSA. The patients took CT scans for 20 seconds with the position of head-first supine. The ScanIP software from Simpleware[®] was used to import the two-dimensional (2-D) CT slice images and then assemble them to the 3-D geometry. Figure 8 shows the 3-D CT image of the patients. For patient A, the original resolution of the CT scan images is 0.475 mm×0.475 mm×1 mm. For patient B, the resolution is 0.467 mm×0.467 mm×0.7 mm. Next, the cubic linear resampling was used to set the 3-D resolution to 0.5 mm³. The position of the end side was determined by the radiologists who took the CT scans on the patients, and most of them have included the whole pharynx. It is noted that the CT scans of those two patients did not include the entire nasal cavity. Therefore, the nasal cavity is not included in the computational domain in the present study.

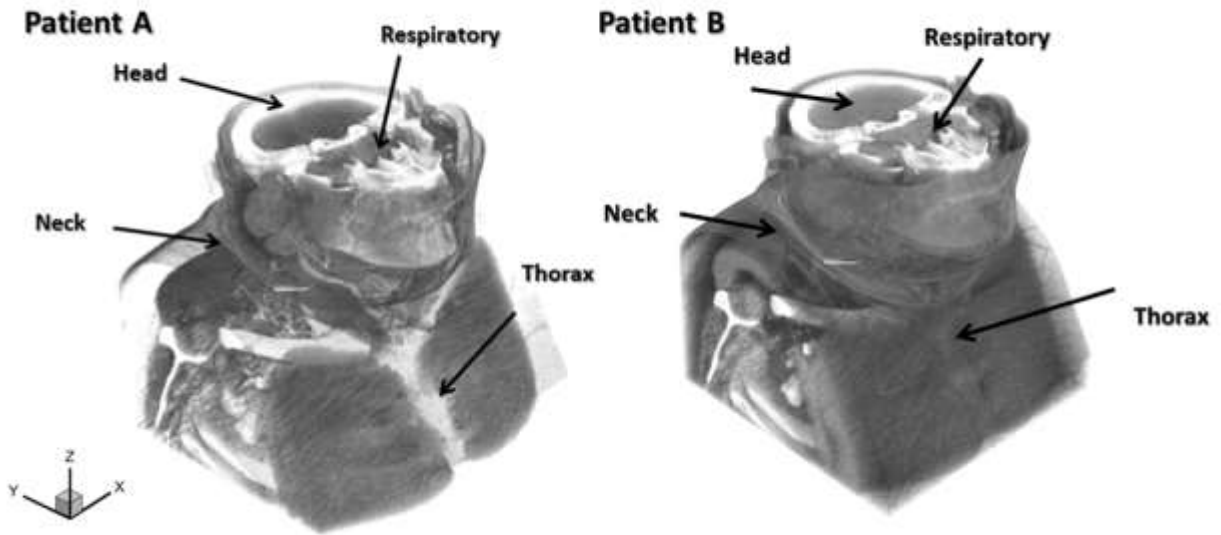


Figure 8. 3-D CT images of patients A and B.

2.2 Segmentation of Airway Tissues and Bones

In the gray-scale CT image, the denser the object is, the lighter the color is shown. For example, the bone is seen as bright white and the air is seen as dark black, with different tissue densities falling in a continuum between these extremes. Because the respiratory tract is distinguishable, it can be easily separated from the rest of the anatomy. This sharp contrast is then used to create the three-dimensional (3-D) geometry of the air tract without surrounding tissues. Figure 9 shows the mid-sagittal plane of the grayscale CT images and their extracted 3-D respiratory tracts, which are the fluid domain, to the right. These two models include the airway in the nasopharynx, velopharynx, oropharynx, and laryngopharynx. These encompass the entire area that may be involved in the airway collapse responsible for OSA.

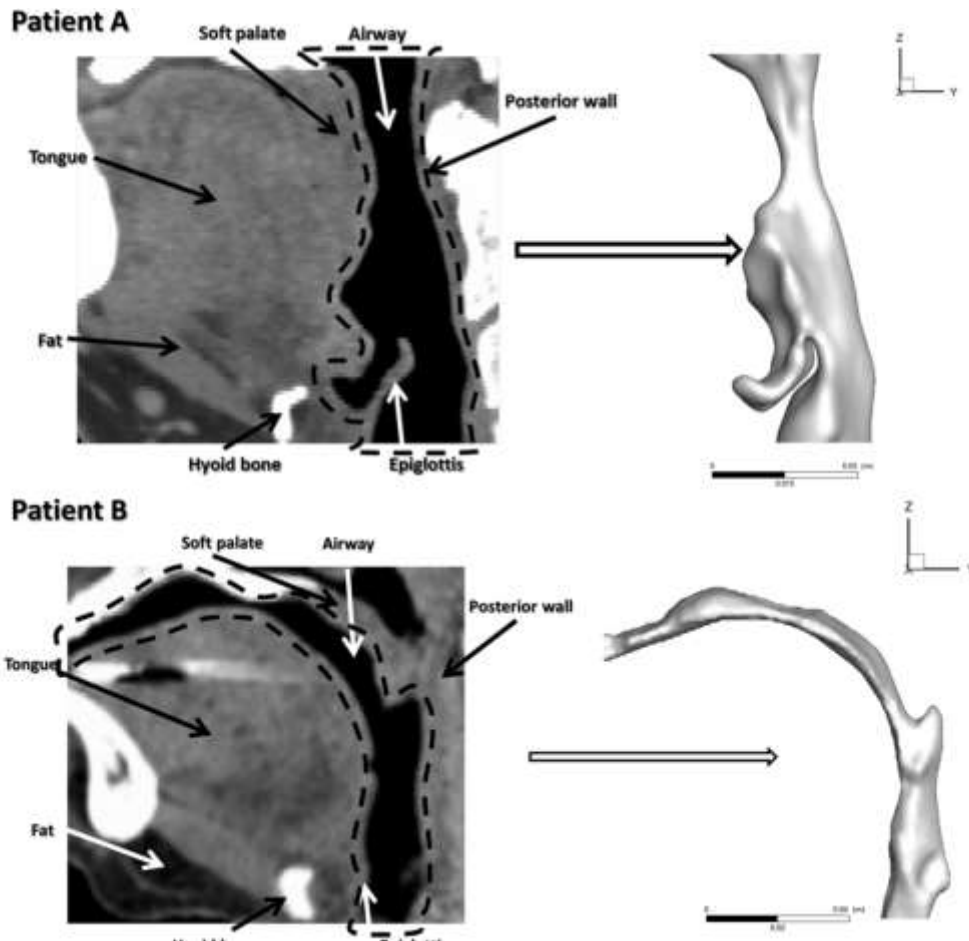


Figure 9. Respiratory tract-the fluid domain for patients A and B.

After the upper respiratory tract is modeled, the soft palate and the tongue are focused on, as they are believed to be the regions that are most possible to collapse. Moreover, the soft palate and the tongue cannot be easily assessed or analyzed without the surrounding tissues, so that the soft tissues under the tongue, hyoid bone, and epiglottis, as well as the surrounding walls, including the lateral and posterior walls, have been considered together in the proposed study models. After manually separated different parts in alternate layers, the ScanIP software was used to

build up the 3-D masks for the tissues and bones, and smooth them with the Gaussian smoothing filter to reduce the human error in the drawing.

For the next step, the 3-D segmented finite element model is built using ScanIP. The compound coarseness slider control is used to control the mesh density, and the element type is set as quadratic tetrahedral. Additional mesh quality improvement has been used to reduce the maximum volume skewness. The tissues that surround the respiratory tract after segmentation are shown in Figure 10. The soft palate is shown in yellow, and the tongue is shown in red. The green denotes the surrounding walls, the ivory represents the bone, and the blue stands for the fat tissues under the tongue. It is very challenging to handle the contact surfaces when there are more than two tissues connecting together at a specific location. In this situation, the surfaces have to be carefully smoothed to prevent sharp corners or tiny island. On the one hand, the geometry of each tissue should be smooth enough to allow the continuous meshing and simulation. On the other hand, there should not be space left between different parts with partial contact. A compromise choice is to leave a few small islands where three or more tissues connect together, so that the contacted tissues can all be smooth. Figure 11 shows the segmented geometry in the 3-D view.

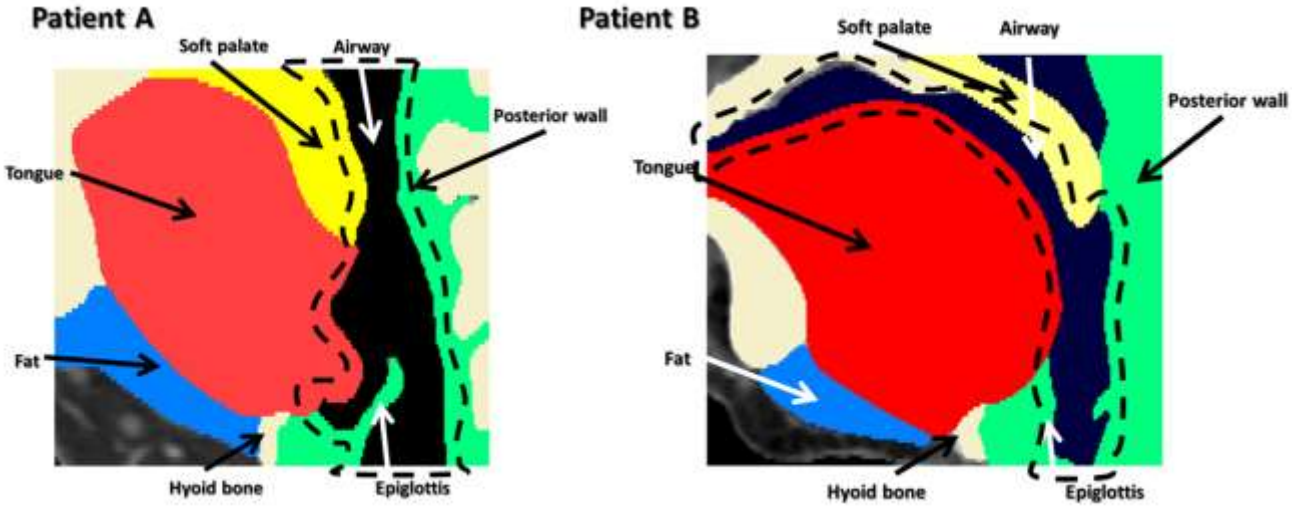


Figure 10. 2-D segmentation of the geometries for patients A and B.

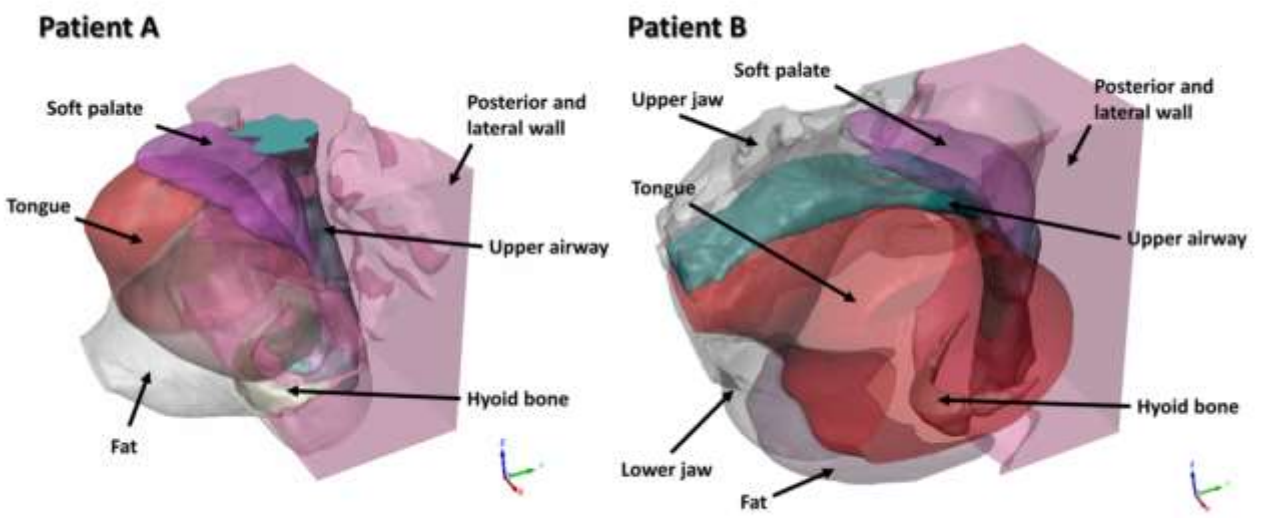


Figure 11. 3-D segmentation of the geometries for patients A and B.

It can be seen that the two patients have different breathing habits. Patient A totally breathes in through the nose. Her soft palate is fully attached to the tongue, which results in no air intake from the mouth. Oppositely, patient B totally breathes air in from the mouth. Her soft palate is closely contacted with the back wall, without letting air intake from the nose. Interestingly, the two patients' physiological structures illustrate two different breathing types. The research has clearly pointed out that breathing through the nose is the correct way, with the most advantages [45, 46]. However, for the sleep apnea patient whose airway is experiencing occlusion, mouth breathing is an alternate way to acquire enough oxygen intake during sleeping.

CHAPTER 3 ELASTICITY EXPERIMENTS

3.1 Specimen Preparation

The respiratory system of a pig is very similar to that of a human because pigs and humans have high physiological and anatomical similarities [47]. Therefore, the pig has served as the valued preclinical specimen for the current research. Five fresh porcine heads weighing about 30 pounds each were obtained from a local butcher shop and stored at 4°C before the experiments, which were conducted within one day of acquisition. The ears and facial fat were removed to facilitate mounting of the heads in different positions on the experimental board, which contains a metal platform with holes that allow the specimens to be securely screwed into place.

3.2 Mechanical Apparatus

The dynamic mechanical analysis (DMA) testing apparatus consists of the Bose 8000 Electroforce test instrument linked to the WinTest DMA software (Bose[®] Corporation, Electroforce System Group, Minnesota, USA) as shown in Figure 12 [48]. The porcine head was immobilized by mounting it on the metal platform with screws in different orientations to allow access to different anatomical structures of the pharynx. For the tissues that could be accessed directly through the mouth, a metal rod with one end mounted on the mobile DMA platform was securely affixed to the specific anatomical structure (i.e. the base of the tongue) on the other end. Dermabond[®] tissue glue was used to securely glue the tissue to the tip of the rod as shown in Figure 13. Alternatively, a metal wire was sewn peripherally into the tested tissue and secured with a metal crimp to avoid slipping of the wire during testing. The free end of the wire was then secured, using the same technique, to the mobile platform of the instrument with the minimal amount of tension to ensure there was no lag in the wire during testing, as shown in Figure 14.

The experimental test was carefully carried out to ensure that the specimen was not damaged or tainted by the traction of the rod or metal wire.

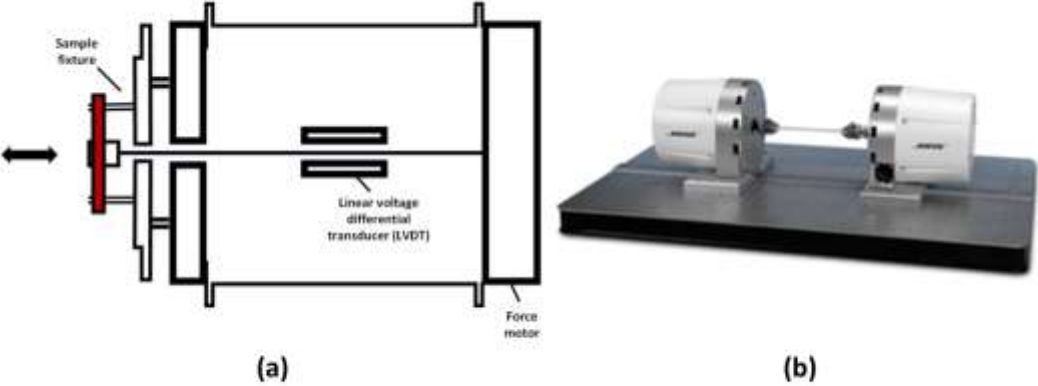


Figure 12. (a) Schematic of the DMA 8000 analytic train; (b) DMA 8000 analytic train [48].

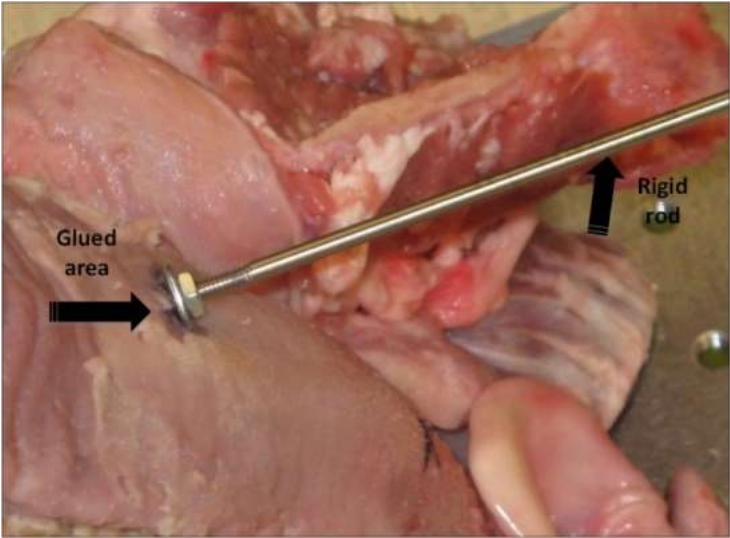


Figure 13. Porcine head fixation and metal rod connection.

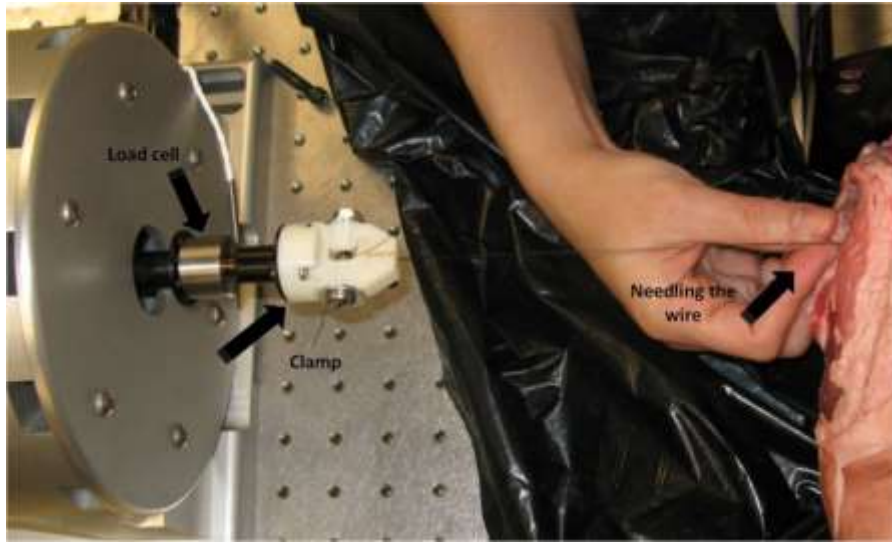


Figure 14. Porcine head and metal wire connection.

3.3 DMA and the Viscoelastic Voigt Model

For each anatomical structure, a 3 mm deformation was requested in the form of amplitude. The force is applied through the DMA instrument until the requested amplitude at several preset frequencies ranging from 1 to 30 Hz is measured. The applied displacement and force were recorded and used to calculate the complex dynamic stiffness K^* , which is the ratio of force to displacement along with a phase angle δ , between the peak force and the peak displacement. The storage and loss stiffness K' and K'' were then derived using Equations (1) and (2).

$$K' = K^*(\cos\delta) \quad (1)$$

$$K'' = K^*(\sin\delta) \quad (2)$$

The storage and loss moduli E' and E'' were obtained by normalizing K' and K'' , respectively,

$$E' = \frac{K^*(\cos\delta)}{S} \quad (3)$$

$$E'' = \frac{K^*(\sin\delta)}{S} \quad (4)$$

where S stands for the shape factor depending on the geometry of the sample. For a rectangular specimen, with width a , height b , and depth l , the shape factor S is calculated as follows:

$$S = \frac{\pi ab}{4l} \quad (5)$$

Most soft tissues exhibit a nonlinear, heterogeneous, inelastic, nearly incompressible, and anisotropic characteristic, which may differ by point and alter with time. However, it may be adequate to model their behavior within the circumstance of the viscoelasticity theory under specific conditions of interest [49]. Soft tissues show both solid-like and fluid-like manners, and they often exhibit characteristic behaviors of viscoelasticity. Since breathing is a cycling process, the pressure exerting on the soft tissues changed nearly sinusoidally based on the change of the intrathoracic pressure from time to time [50]. The deformation of the tissue lags behind the force. The viscoelastic properties can precisely describe those hysteresis phenomena and are also considerably beneficial for the FSI simulation.

The viscoelastic Voigt model, as shown in Figure 15, is one of the viscoelastic models that presents the parallel combination of a linear spring with modulus of elasticity E and a dashpot with viscosity μ , which has previously been shown to describe the viscoelastic response of the biological tissue [51]. It can be used to describe the UA tissue properties obtained from the experimental measurements,

$$\sigma = E\varepsilon + \mu\dot{\varepsilon} \quad (6)$$

where σ is the stress, μ is the viscosity of the dashpot, E is the Young's modulus, ϵ is the strain, and $\dot{\epsilon}$ is the rate of change with respect to time.

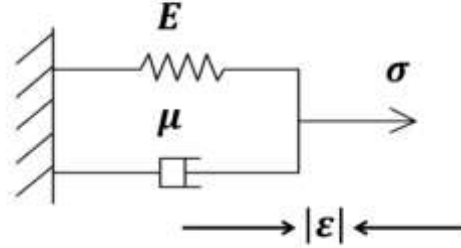


Figure 15. Viscoelastic Voigt model of the tissue.

The complex dynamic modulus E^* can be calculated using Equation (7),

$$E^* = E' + iE'' = E + i\mu\omega \quad (7)$$

and the phase angle of the complex modulus is defined as follows,

$$\delta = \tan^{-1}\left(\frac{E''}{E'}\right) = \tan^{-1}(\omega\mu/E) \quad (8)$$

3.4 Validation of Constrained Method against Previous Studies

For elasticity measurements, it is essential that the samples remain unconstrained or unconfined laterally as they are tensed or compressed axially. If the sample is constrained laterally, then the constrained Young's modulus will be larger than the unconstrained Young's modulus [52]. Constrained experiments are requisite to be validated since the elasticity from the constrained method has not been performed by previous researchers. Standard unconstrained experiments

were carried out using resected (free) porcine middle tongue tissue and compared to the results from the previous publications. Cuboid pieces of tongue were cropped and fixed between the mobile DMA arm and the immobile platform with one plastic clamp on each side, as shown in Figure 16. Samples were carefully oriented to assess both anterior-posterior (AP) and superior-inferior (SI) planes.

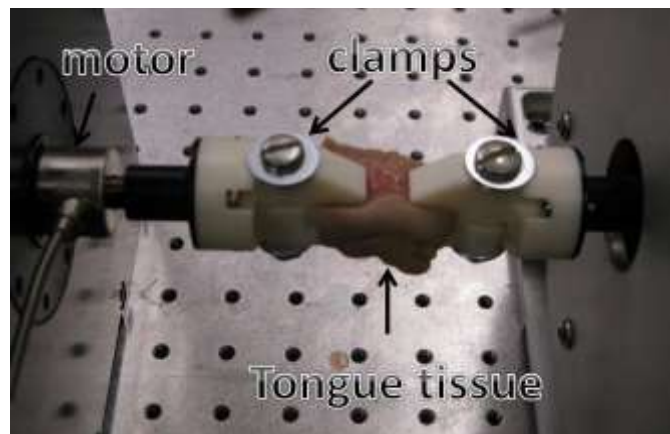


Figure 16. Unconstrained measurements: porcine tongue tissue being held between plastic clamps.

The constrained experiments were carried out with the porcine mandible mounted on the test bed as shown in Figure 17. In this configuration, the maxilla (upper jaw bone) and superior structures were removed, and the mandible (lower jaw bone) and inferior structures were isolated, so the tongue maintained its attachments to the surrounding soft tissues and bony supports. Dermabond[®] glue was used to adhere the base of the tongue to a 0.91 cm diameter round surface

at the end of the 20 cm long stainless steel lever arm of the DMA instrument. The axial stress was applied to different regions of the tongue with this technique.

From these experiments, the Poisson's ratio of the tongue was calculated using the formula as follows:

$$Y_0 = Y_b \left(1 - \frac{2\nu^2}{1 - \nu}\right) \quad (9)$$

where Y_b denotes the unconstrained Young's modulus, Y_0 stands for the constrained Young's modulus and ν represents the calculated Poisson's ratio [52].

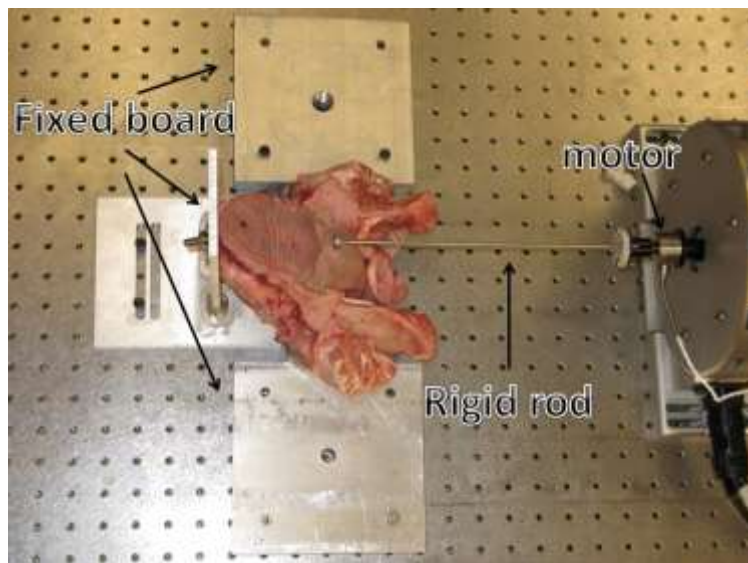


Figure 17. Constrained measurements: porcine tongue tissue intact with the lower jaw.

The Poisson's ratio was found to be 0.497, with an error of 1.4%, compared to the common value of 0.49 reported by other researchers [53, 54]. In addition, the Young's modulus calculated

from the constrained experiments is averaged to a value of 4822.8 Pa. This obtained value of stiffness is medium compared to previously published moduli obtained by other researchers using magnetic resonance enterography (MRE) or compress method, as shown in Table 1. Therefore, the obtained experimental results are validated, and the constrained measurements are able to acquire the viscoelasticity of other tissues. Two assumptions have been made here: firstly, the porcine tissue has the same stiffness as human tissue; secondly, the resultant force deviation from the long thin rod in the experiment is omissible. The near-wall tissues, such as the soft palate, pharyngeal walls, and fat under the tongue, are hard to be sectioned and properly placed between clamps. The constrained method is more flexible to test these anatomical structures with different ways of attachment.

Table 1. Comparison with the Young's modulus from other researchers.

Reference	Young's modulus of tongue (Pa)	Method
Cheng et al. [53]	8010	MRE (magnetic resonance enterography)
Malhotra et al. [55]	6000	Ex-vivo
Xu et al. [56]	3500	Ex-vivo
Payan et al. [57]	15000	Ex-vivo
Gerard et al. [58]	1140	Ex-vivo
Present study	4822.8	Ex-vivo

3.5 Specially Designed Testing for the Epiglottis

Similar unconstrained experiments were carried out for the walls of the UA, including the lateral and posterior pharyngeal walls, which have different bony attachments leading to various degrees of stiffness. The soft palate and fat under the tongue were also tested using the unconstrained method because the tissues are too small to be placed between the clamps. Since soft tissues are mainly composed of water, they can be considered as the quasi-incompressible material. On account of the simplicity, the value of 0.49 is used as the Poisson's ratio for all soft tissues [53, 54], and the Poisson's ratio of 0.3 is used for the epiglottis cartilages [39].

Different from other tissues, the epiglottis is mainly cartilage. Notably, the tip of the epiglottis moves in an anterior-posterior way to block the trachea while swallowing. The experiment for the epiglottis is carried out when the left side, right side, and bottom side of the epiglottis are all fixed, and the wire penetrating through the epiglottis is used to drag from the tip of the epiglottis, as shown in Figure 18.

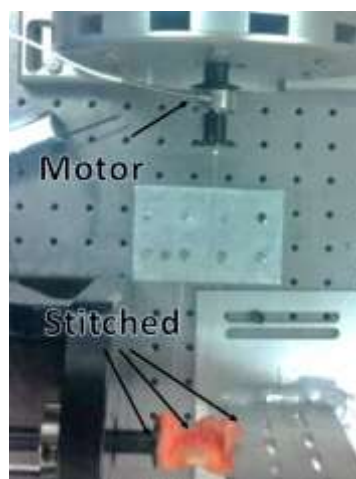


Figure 18. Unconstrained measurements: epiglottis cartilage.

3.6 Results and Discussions

3.6.1 Tissue test in lateral and axial directions

A cubically shaped tissue cut from the middle of the tongue was tested in both anterior-posterior (AP) and superior-inferior (SI) planes to calculate the Young's modulus in both lateral and axial directions. The obtained results are shown in Table 2. Not surprisingly, the elasticity of the tongue was found to be anisotropic, with a distinctive difference of 68.87% in the Young's modulus between the AP and SI directions. The tongue is made up of several muscles with fibers organized into bundles that run in different directions at different depths [59, 60]. This unique anatomic feature likely accounts for the anisotropic elasticity of the tongue tissue, as the compliance of the tissue is different depending on whether the force is applied along or across the muscle bundle.

Table 2. The Young's modulus of the middle of the tongue from the unconstrained experiment.

	Young's Modulus Anterior Posterior (AP)	Young's Modulus Superior Inferior (SI)
Trial 1	3700 Pa	1016 Pa
Trial 2	3220 Pa	995 Pa
Trial 3	3016 Pa	1082 Pa
Average	3312 Pa	1031 Pa
Standard Deviation	351 Pa	45.4 Pa

Comparing the two planes in the anatomically intact model, the most substantial and important movements of the tongue are expected to be in the AP plane, which is also the major movement that causes airway narrowing in the patient with sleep apnea symptoms. Therefore, these AP calculations are assumed to be the most critical data for the numerical simulation. In this present study, for simplification, the tongue is assumed as the isotropic material with the elasticity in the AP direction. In the future work, the anisotropic elasticity of the tongue should be studied for a more precise and realistic model. As mentioned by Yousefi et al., tongue as a combination of various muscles surrounded by the mucous membrane is a complicated architecture to study [61]. To study the anisotropic elasticity of the tongue, the properties of different muscles and mucous need to be studied, and the research in this field has not been fully established. Proper constitutive models need to be developed for each muscle and mucus, too.

Moreover, this comparison showed an advantage of *ex vivo* experiment over magnetic resonance enterography (MRE). The former can be used to conduct the test on a particular spot in any specific direction, while the latter can only be used to capture the stiffness based on the graphics, without considering the directional difference.

3.6.2 The constrained Young's modulus vs. frequency

The constrained Young's modulus vs. requested frequency is shown in Figure 19. It can be found that the constrained Young's modulus is dependent on frequency, which it dramatically increases when the frequency exceeds 20 Hz. This feature may be explained by the fact of that the interactions among the actin, elastin, resilin, and abductin in the tissue can lead to protein-protein network-like structures when the frequency is suddenly increased [54]. Since the normal human breathing rate is 15-20 times/minute, the Young's modulus at 1 Hz can be designated from the experiments, and it can be used in the present FSI simulation.

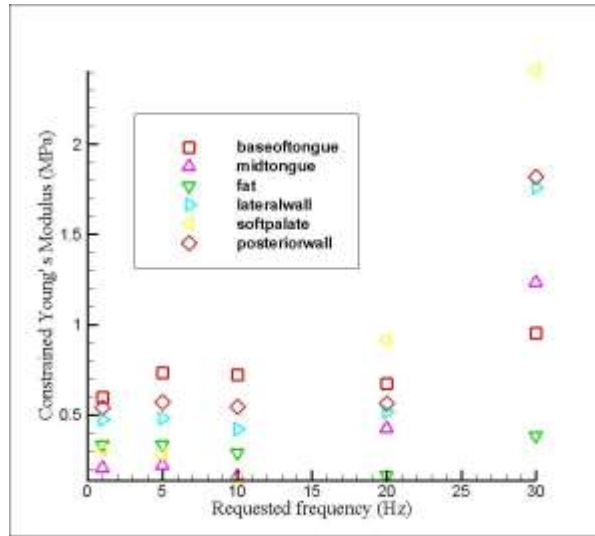


Figure 19. Comparison of the constrained Young's modulus at different requested frequencies.

3.6.3 The Young's modulus calculated from the constrained measurements

Table 3 displays the data calculated from the constrained Young's modulus of the different tissues tested at the frequency of 1 Hz and the requested deformation of 3 mm.

Table 3. The Young's modulus calculated from the constrained measurements (@ 1 Hz, 3 mm).

Position	Young's modulus E^* (Pa)	Storage Modulus E' (Pa)	Loss Modulus E'' (Pa)
Base of tongue	5984.2	4822.8	3537.2
Upper tongue	2959.9	2717.3	1170.5
Soft palate	3127.8	2897	876.82
Lateral wall	4705.1	4379.1	1715.6
Posterior wall	5417.4	5010	2055.3
The fat	3346.8	3216.8	920.02
Epiglottis	31942.5	30822	8350.5

From these data, it can be found that the tissues have distinct degrees of elasticity that correlate with intrinsic tissue characteristics and connections to surrounding structures. For example, the body of the tongue (the most anterior portion of the tongue in its anatomical position) was found to be the most elastic, which correlates with its untethered nature, and it is free to move in several different directions. The soft palate was also found to be a relatively lenient structure, which corresponds with a single, broad bony attachment (to the hard palate) at the anterior face of the structure, while the posterior portion and uvula dangle into the oropharynx. Additionally, the soft palate consists of mucosa lining very thin layers of the muscle, which provides minimal resistance to stretch. The submandibular tissue, taken as the single entity in its anatomical position, was found to be stiffer than both the tongue and soft palate from the experiments. This finding is interesting, as the submandibular space is mainly composed of fatty tissue and glands that are loosely associated and can be easily dissected from each other. The stiffness of this area can be explained by the encasing mucosa and muscle, which is tethered tightly to the mandible under the tongue. The individual tissues, therefore, do not act as separate objects; instead, they are enveloped as a single “package” that is unable to expand as freely as the individual pieces if the test were done separately.

The base of the tongue, which is considered to be the principal structure involved in UA collapse for OSA patients during sleep, was found to be the most unyielding soft tissue of all tested. It correlates well with its tightly tethered position to underlying bony structures and thick musculature makeup.

The epiglottis was calculated to be five times stronger than the base of the tongue. This may explain the fact of that most sleep apnea patients have suffocation at the base of the tongue instead of the epiglottis, which looks like a swing part from the CT scanning. In the later study,

in Chapter 4, the two-way FSI system coupling simulation was conducted to provide detailed movement at the tip of the epiglottis to illustrate this phenomenon.

3.6.4 The advantage and limitation of constrained experiments

This is a pilot study to investigate the viscoelastic properties of porcine UA using constrained methods. Traditional unconstrained experiments need to cut the samples down and fit them into the testing instruments. The vital benefit of the constrained test method is that the tissues were tested exactly with their surroundings in reality. Because of the existence of the stress from the surrounding tissues, the constrained results could be more realistic and reliable. Furthermore, since the properties of the tissue can be tested without cutting it off from the whole body, under the premise that there is enough space to conduct the experiment, even living human tissues could be tested with only slight epidermal damage. However, everything has two sides. The constrained experiment also has its limitations. It always shows that the extent of deformation is higher than the expected value because deformations from other skin, nerves, and muscles are all added to the tested tissue under the given force. Moreover, deviation should always be taken into account when a testing rod is used.

3.6.5 Precondition

In the tissue experiment, the preconditioning procedure is a very important step. The reason why the preconditioning procedure is needed for the tissue specimen, or why the load-elongation curve might shift, is because the internal structure of the tissue could change with the cycling [54]. After the tissue is tested on the testing machine, the researchers need to test for the load-elongation curve by loading and unloading at a constant or a slowly changing frequency, then let

the tissue be rested about 10 min, and repeat the same procedure. This difference will decrease after the tests are repeated several times, which is called the preconditioning procedure.

3.6.6 Reasons for the difference compared to the published data

Firstly, the characteristics of the soft tissue not only differ by point, but also vary with time [62]. The soft tissues show both solid-like and fluid-like manners and they often exhibit viscoelasticity behaviors. Although the viscoelasticity properties can be determined by *in-vivo* and *ex-vivo* experiments, these values show great variation in viscoelastic parameters for different human or animal tissues. Secondly, most *ex-vivo* experiments are tested with human cadavers, which have a variety of changes occurred after death. Stiffening of muscles is well recognized and is known as algor, livor, and rigor mortis, respectively. Unfortunately, the time frame for such changes has great variation among individuals. It usually begins within several hours of death, maximizes at 6-12 hours, and is thought to pass off by approximately 50 hours [63]. Temperature, humidity, reason of death, time of being frozen and unfrozen, length of experiments, and so on, are all factors adding to the unpredictability to the viscoelastic properties of the tissue. Thirdly, porcine cadavers were used in the present study, and there could be a difference between human and porcine tissues. All these reasons can possibly explain why there are some variations compared to the published data.

3.6.7 Future use of the constrained method

The key point in this experimental study is to use constrained measurement to calculate the Young's modulus for different tissues in the UA; whereas other researchers only tested the tongue and soft palate. Hereafter, the obtained results from the measurement data can be used in the present two-way FSI numerical simulation. Furthermore, the testing method can be used in

other tissue tests, or other material tests, which are not easily tested unconstrainedly, or need to be measured in some special circumstance. Using MRE, it is possible to test the properties that belong to the tissue/cartilage; however, using *ex-vivo* constrained experiments, one may find more realistic and reliable results, which can be related to the surrounding tissues.

3.6.8 Viscoelasticity vs. linear elasticity

As mentioned in section 3.3, a viscoelastic material has an elastic component and a viscous component, while an elastic material only has an elastic component. An elastic material does not dissipate energy when a load is applied and removed. However, a viscoelastic material loses energy when a load is applied and removed. Figure 20 shows the load-displacement curve of the epiglottis at the tested frequency of 1 Hz. The hysteresis loop in the load-displacement curve shows the amount of energy loss in a loading and unloading cycle. The small hysteresis area shows that the energy loss through a loading cycle is relatively small compared to the total energy storage. In addition, the relation of the load and displacement is close to a linear relation, especially during the loading process, which has a maximum error of 0.09 N at $d = 2.97 \text{ mm}$, and the coefficient of determination is $R^2 = 0.989$. The unloading process has a maximum error of 0.30 N at $d = 1.78 \text{ mm}$ and a coefficient of determination $R^2 = 0.686$, which represents a larger but acceptable degree of linear correlation. Moreover, linear load-displacement relation results in linear stress-strain relation, which can be used to simplify the constitutive equations and save the computational cost. As a result, the viscoelasticity was simplified as linear elasticity in the later simulation.

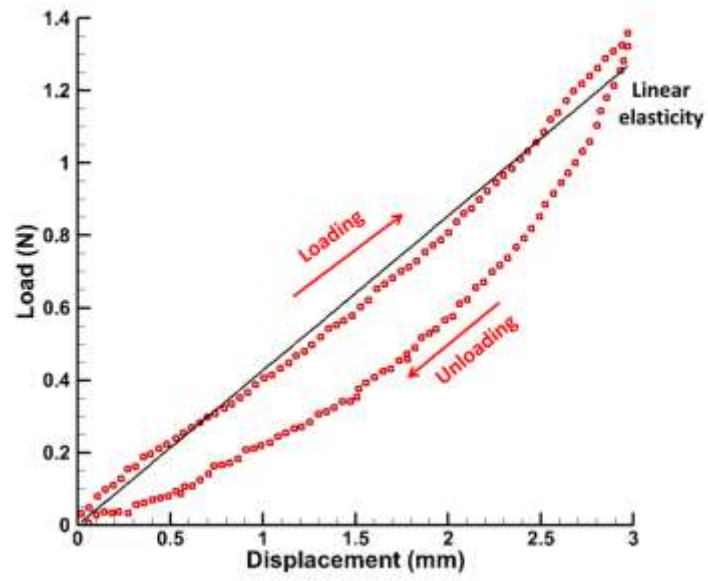


Figure 20. Load-displacement curve of the epiglottis at the tested frequency of 1 Hz.

CHAPTER 4 FLUID-STRUCTURE INTERACTION NUMERICAL MODELING

4.1 Coupled System and Governing Equations

For the fluid domain, the estimated maximum Reynolds number is calculated with Equation (10) based on the air density of 1.138 kg/m^3 at 37°C , average velocity of 1.95 m/s , hydraulic diameter of 0.0188 m (calculation based on area and parameter at inlet of the UA at nasal cavity), and dynamic viscosity of air of $1.77 \times 10^{-5} \text{ kg/m} \cdot \text{s}$,

$$Re = \frac{\rho \bar{v} d}{\mu} = 2357 \quad (10)$$

which indicates the fluid flow inside the UA to be transitional. The standard k- ω turbulence model is appropriate to be used to simulate this complex flow [38].

The fluid sub-problem is governed by the incompressible Navier-Stokes equations [39-44], under the Arbitrary Lagrangian Eulerian (ALE) framework in the deformable domain Ω^F . The velocity $\vec{u} = \vec{u}(x, y, z, t)$ and the pressure $P = P(x, y, z, t)$, inside the fluid domain at time t are expressed as follows:

$$\nabla \cdot \vec{u} = 0 \quad (11)$$

$$\frac{\partial \vec{u}}{\partial t} + (\vec{u} \cdot \nabla) \vec{u} = \nu \nabla^2 \vec{u} - \frac{1}{\rho_f} \nabla P \quad (12)$$

where ρ_f is the fluid density, \vec{u} is velocity vector, ν is the kinematic viscosity.

The standard k- ω turbulence model that is used as the closure for the Reynolds-averaged Navier-Stokes (RANS) equations is shown below,

$$\frac{\partial k}{\partial t} + \frac{\partial}{\partial x_j} (u_j k) = \tau_{ij} \frac{\partial u_i}{\partial x_j} - \beta^* k \omega + \frac{\partial}{\partial x_j} [(v + \sigma^* v_T) \frac{\partial k}{\partial x_j}] \quad (13)$$

$$\frac{\partial \omega}{\partial t} + \frac{\partial}{\partial x_j} (u_j \omega) = \alpha \frac{\omega}{k} \tau_{ij} \frac{\partial u_i}{\partial x_j} - \beta \omega^2 + \frac{\partial}{\partial x_j} [(v + \sigma v_T) \frac{\partial \omega}{\partial x_j}] \quad (14)$$

where k is the turbulence kinetic energy and ω is the specific rate of dissipation of kinetic energy, $v_T = \frac{k}{\omega}$ represents the kinetic eddy viscosity, α , β , β^* , σ , σ^* are closure coefficients developed by David C. Wilcox [64], and $\alpha = 13/25$, $\beta = 9/125$, $\beta^* = 9/100$, $\sigma = \frac{1}{2}$, $\sigma^* = 3/5$ are used in the present study.

For small deformation, linear relationship between the stress and strain, with no yielding produced, the structure sub-problem under the Lagrangian framework in the reference domain Ω^s is governed by the linear constitutive relations, which can be expressed in tensor notation as: the equations of motion,

$$\rho_s \frac{\partial^2 d_i}{\partial t^2} = \frac{\partial \sigma_{ij}}{\partial x_j} + F_i \quad (15)$$

the strain-displacement equations,

$$\epsilon_{i,j} = \frac{1}{2} \left(\frac{\partial d_j}{\partial x_i} + \frac{\partial d_i}{\partial x_j} \right) \quad (16)$$

the constitutive equations for isotropic homogeneous material,

$$\sigma_{ij} = \frac{E\nu}{(1+\nu)(1-2\nu)} \epsilon_{kk} \delta_{ij} + \frac{E}{(1+\nu)} \epsilon_{ij} \quad (17)$$

where F_i is the force, d_i is the structural displacement, t is the time, ρ is the density, σ_{ij} is the solid Cauchy stress tensor, ϵ_{ij} is the strain, ν is the Poisson's ratio, and E is the Young's modulus.

The two-way FSI coupling procedure is characterized by iterations between the deformable structure and the internal fluid flow. Commencing with the fluid flow field, the interface loads are calculated and applied to the solid domain, which is then solved to extract the wall displacement to update the fluid domain. The domains are updated and solved until the two solutions reach an agreement with a given relative tolerance of 1×10^{-3} .

4.2 Boundary Conditions

The setup of the boundary conditions is critical and important to obtain the correct solution. In previous publications [41, 43], either pressure inlet/outlet, or flow rate inlet have been used as boundary conditions. Cheng et al. [35] pointed out that the outlet pressure varies by each patient's specific UA geometry. Gupta et al. [65] studied the volumetric flow rate range regarding weight. It has been concluded that both the pressure and the flow rate is not a fixed value for everyone, and they both changed within a range. The pressure difference between the inlet and outlet varies from several pascals to several hundred pascals, and the flow rate varies by body weight, gender and severe level of illness. One method used by several former researchers [41-43] is to ramp up one parameter and double check the other parameter to see whether it is in the right range. Compared using pressure with using flow rate as the boundary condition, the results only have a difference at the inlet, since the velocity is averaged at the inlet using the flow rate boundary condition. Since using the pressure boundary condition provides a faster convergence rate [66], the flow simulations are performed while ambient static pressure conditions are set at the inlet of the computational domain (pharyngeal plane). The outlet pressure was set to vary in the sinusoidal fashion from 0 Pa to -2000 Pa and back to 0 Pa in 1.66 s. Normal people have three breaths in ten seconds, so each breath in process roughly takes $3.33/2 = 1.66$ s. The turbulence intensity of 6.02% was calculated from Re and used for the

simulation. On the surrounding walls of the UA, the Dirichlet boundary condition of velocity $\vec{u}(x, y, z, t) = \vec{0}$ is used, which represents the no-slip boundary condition. Smoothing and remeshing methods are used for fluid and structure interface deformation during the dynamic simulation process. The coupling between the pressure and the velocity fields is implemented through the semi-implicit method for pressure-linked equations (SIMPLE) algorithm [67]. The uniform time step of 0.001 s is applied, which can provide accurate two-way FSI coupling results within the reasonable computing time [68].

For the boundary condition of the tissues, the surfaces in contact with the spine, hard palate, and lower teeth are set as constraints. With the Dirichlet boundary condition, the displacement vector is $\vec{d}(x, y, z, t) = \vec{0}$ and the hyoid bone is free to move horizontally in the x-y plane. The upper and lower boundaries are constrained in the z-direction and free to move in the x-y plane. The airway walls are set as the coupling interface,

$$\vec{u} = \frac{\partial \vec{d}}{\partial t} \quad (18)$$

$$\sigma^f \cdot \vec{n}^f = \sigma^s \cdot \vec{n}^s \quad (19)$$

where σ^f and σ^s are the Cauchy stress tensor in the Newtonian fluid field and in the structural field, respectively, and \vec{n}^f and \vec{n}^s are the normal vectors.

Also, the contact between the soft palate and the tongue is crucial in considering the soft palate and the tongue movement. This contact relation is described by frictionless contact. In this study, the gravitational acceleration is not added externally because the CT was taken when the patient was lying down, which means the effect of gravity was already taken into account in the original geometry. The density of the soft tissues and bones are 1100 kg/m³ and 1850 kg/m³,

respectively, based on the experimental data obtained from fresh porcine head cadavers [69]. The Poisson's ratio is set as 0.49 based on the soft tissues being considered as roughly incompressible materials. The Young's moduli used for the soft palate, tongue, fat, and surrounding walls are set as those values listed in Table 3. The Young's modulus and the Poisson's ratio for the bones are 1.37×10^{10} Pa and 0.3, respectively [39]. Xu et al. [56] compared the linear and nonlinear material models. The relative error in the strain was less than 5% over the stretch ratios up to 1.19 [56], while in the present work the stretch ratio is less than 0.1.

4.3 Solver Settings

The fluid simulation was done using ANSYS[®] Fluent 17.2. The pressure-based solver is used with the absolute formulation for the velocity field. The standard $k-\omega$ turbulence model was selected with 6.02% backflow turbulent intensity and 0.02 m as the hydraulic diameter, which was calculated at the inlet of the UA at the nasal pharynx. The SIMPLE algorithm was used to solve the pressure-velocity coupling, and the spatial discretization of the pressure and momentum are both second order; the spatial discretization of the turbulence kinetic energy and the dissipation rate are both first order. Humid air is used as the working fluid with a constant density of 1.24 kg/m^3 and the dynamic viscosity of $1.79 \times 10^{-5} \text{ kg/m} \cdot \text{s}$. The solid mechanic simulation was done with using ANSYS[®] transient structural 17.2. The direct sparse solver is used with numerical damping control. The Newton-Raphson residual is set as 4, and the large deflection is turned on. The two-way system coupling is done with the ANSYS[®] workbench 17.2, where the interface loads from the fluid flow field are calculated and applied to the solid domain, which is solved next to extract the wall displacement to update the fluid domain. The domains

are updated and solved until the two solutions reach an agreement with a given relative tolerance of 1×10^{-3} .

4.4 Mesh Independence Study

The 3-D fluid sub-model of patient A is meshed using the Simpleware[®] ScanIP software with linear tetrahedral elements, as shown in Figure 21. The fluid-solid interface is selected for mesh refinement in order to obtain a better description of the boundary layer velocity gradient. The boundary layer mesh has four layers with the viscous layer thickness less than 0.2 mm, where the dimensionless wall distance y^+ is controlled below 5. To establish the validity of the CFD solutions, a mesh independence study was performed. Five different node densities, with node numbers 4985, 5954, 8811, 24307, and 76805, were studied, and a straight line from the inlet to the outlet was chosen from the fluid field (including inlet, outlet, high-speed area, and near wall area) to compare the computational solution, as shown in Figure 22. As the mesh becomes finer, the velocity and pressure are barely influenced by the nodes' density. The fine mesh with 24307 nodes and 17805 4-node tetrahedral elements, which shows the percentage error less than 3%, is the optimum mesh on the premise of guaranteeing the quality of the numerical solution. Similarly, a mesh study with the 3-D structure sub-model was accomplished. The tetrahedral elements were employed due to the complex morphology of individual tissue components although the hexahedral elements are preferred for modeling the nearly incompressible materials. The structural meshes with the number of quadratic tetrahedral elements of 255665, 575457, 1514290, and 2799865 were compared, and the second one, with 575457 tetrahedral 10-node elements was selected for simulation, with which the percentage error is less than 3%.

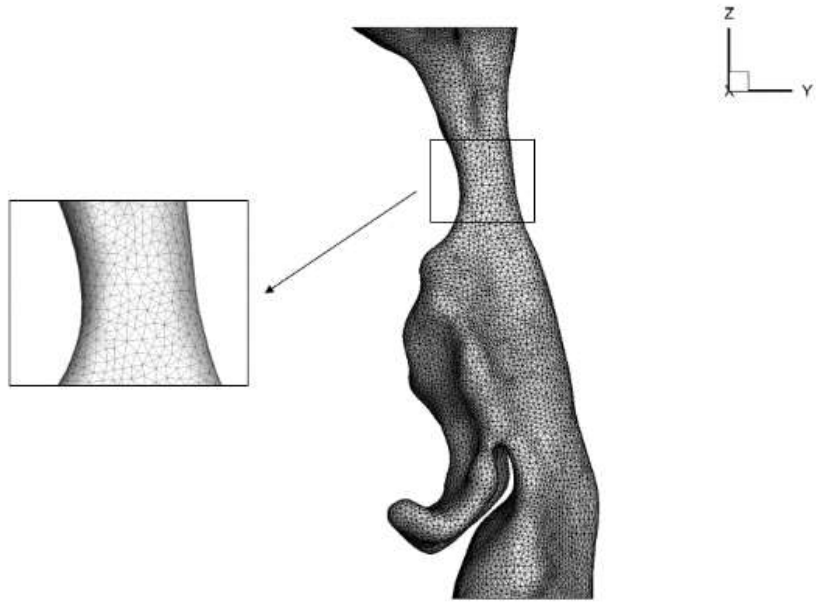


Figure 21. Meshed fluid geometry based on patient A.

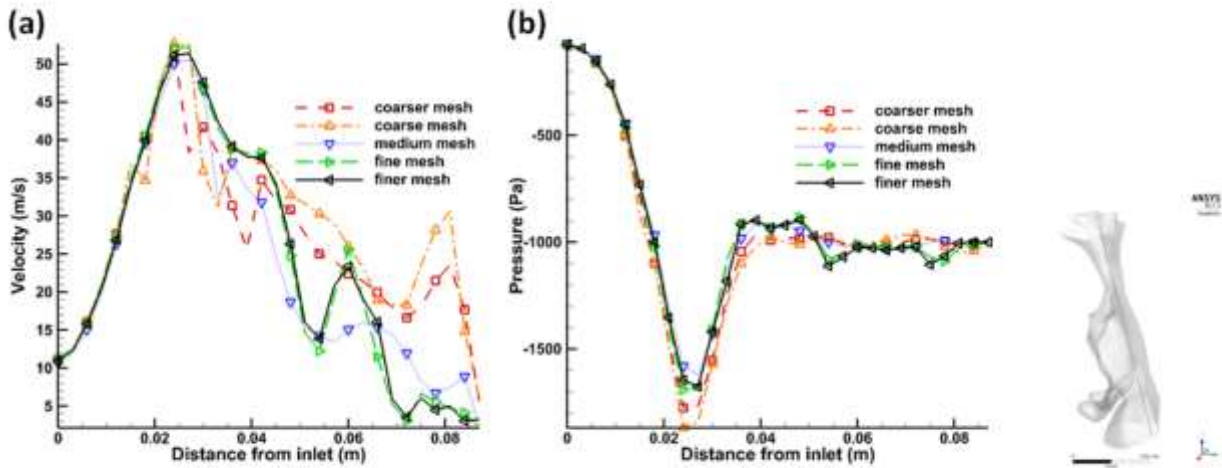


Figure 22. Comparison of (a) velocity and (b) pressure distribution along the typical line computed using different mesh resolutions based on patient A.

CHAPTER 5 STUDY OF UPPER AIRWAY COLLAPSE

5.1 Investigation of Velocity Field in the Pharynx

Figure 23 (a) ~ (d) shows the velocity streamlines at four different instants $t=0.1$ s, 0.2 s, 0.3 s, and 0.35 s of the inhalation process, respectively, based on patient A. As shown in Figure 23, the jet flow [70] was formed when the cross-sectional area dramatically decreased from the nasopharynx to the velopharynx, and largely increased from the velopharynx to the oropharynx. The maximum speed of the jet flow in this study is about 65.8 m/s, and the Mach number is about 0.19. Since the Mach number is less than 0.3, the incompressible flow assumption can be properly used in the present study. As shown in Figure 23, a major recirculation occurs below the most restricted region of the airway, which is located right after reopening into the oropharynx. This recirculation flow at the oropharynx is formed by the flow separation in the hypopharynx. The separated flow later traveled back to the oropharynx with strong circulating movement within this region. Then the kinetic energy was passed to the eddies with smaller length scales and was converted to heat by viscous dissipation. A minor recirculation region was formed where the airway narrows around the epiglottis. A smaller swirl was formed between the epiglottis and the base of the tongue. As a result, this recirculation region also dissipates the kinetic energy of the flow.

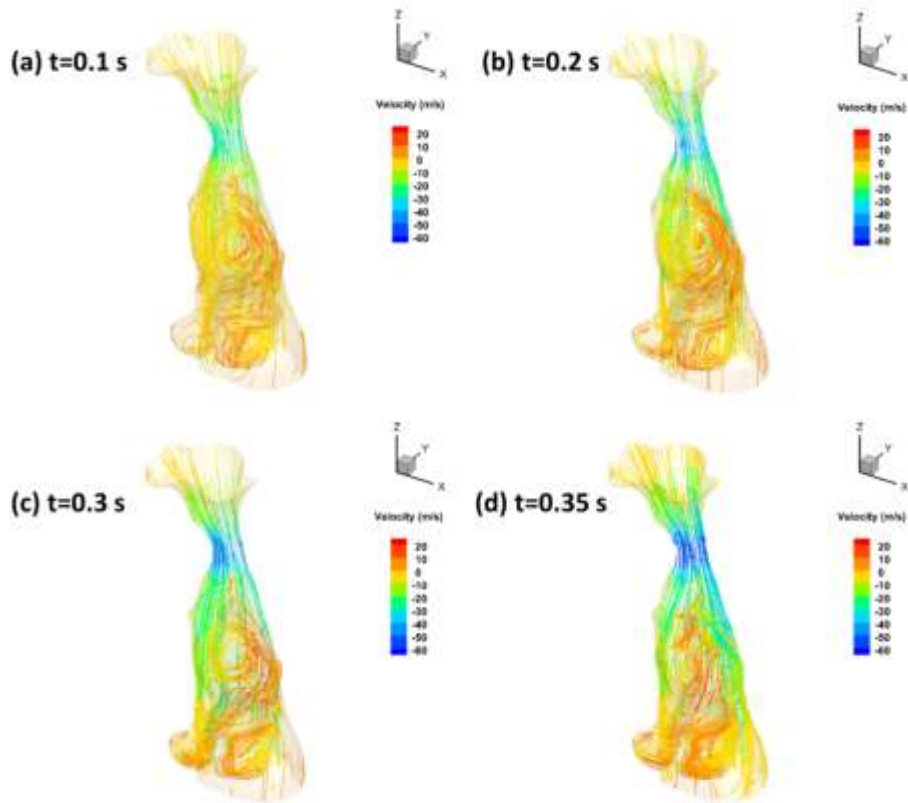


Figure 23. Velocity streamlines in the upper airway at different times (a) 0.1 s, (b) 0.2 s, (c) 0.3 s, (d) 0.35s based on patient A.

5.2 Investigation of Wall Shear Stress

The wall shear stress (WSS) distribution is studied along the polyline, where the posterior wall and the mid-sagittal plane intersect. As shown in Figure 24, from 0 to 0.3 s, the shear stress increases obviously as the pressure difference between inlet and outlet increases. From 0.3 s to 0.35 s, the WSS decreased in the velopharynx region, but it continually increased in the collapsing region behind the tip of the soft palate. This is because when the tip of the soft palate

moved toward the back wall it caused the middle of the soft palate to be slightly bent. Then it can relatively enlarge the cross-sectional flow area in the velopharynx region.

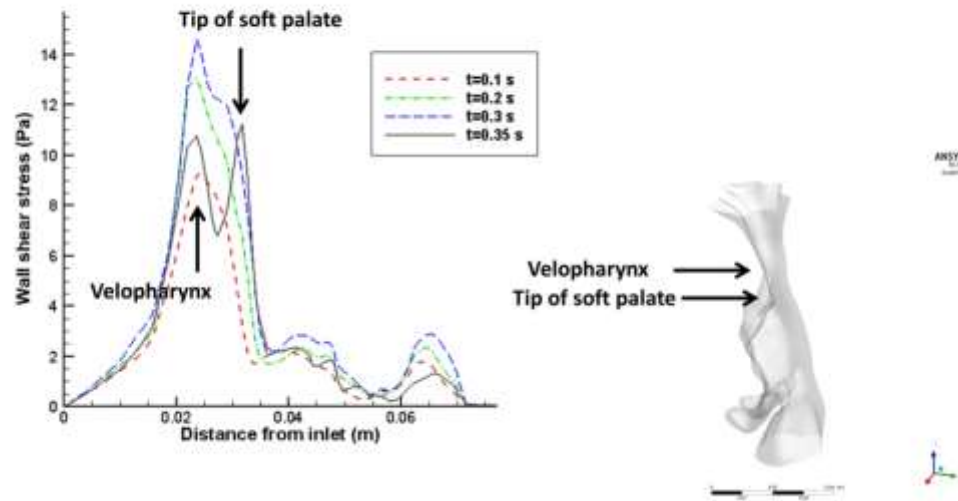


Figure 24. Wall shear stress along the anterior polyline (intersection of the sagittal plane and the FSI interface) based on patient A.

5.3 Investigation of Pressure Field in the Pharynx

The pressure contour of the horizontal cross-sectional planes is shown in Figure 25 (a) ~ (d). It demonstrates the low-pressure region at the pharynx, especially at the tip of the soft palate. Based on the Bernoulli's theory, the high velocity flow would result in low static pressure. As the pharyngeal pressure went lower, the pressure difference between the inner air pressure and the outer ambient pressure dramatically increased, and this pressure difference can gradually

cause the upper airway to collapse. The pressure gradient in the oropharynx was larger than other regions on account of the pharyngeal jet so that the major recirculation zone occurred in this region. As time went forward, the tip of the soft palate gradually moved closer to the side wall until they were fully touching. The soft tissue would further move back until the UA was fully collapsed. As mentioned by Cheng et al. [53], the pressure distribution varies from person to person due to the different shape of the UA. It is important to conduct a patient-specific simulation for each patient. Solving such a largely deformed geometry normally requires a long time and high computational cost, but using the curve fitting the simplified prediction of the time for the airway to collapse can be obtained, as shown in Figure 26. Based on the polynomial curve fitting, it can be predicted that at the time 0.37 s, the tip of the soft palate will contact the side wall; at the time 0.4 s, the airway will fully collapse at the tip of the soft palate region, while the flow area of the collapsing region becomes zero. When the airway is fully collapsed, the patient is still in the middle of the inhaling process. This means patient A's UA will not open immediately, because she has not breathed in enough air yet. This correlates with the fact that patient A has been diagnosed with severe OSA. If the suffocation persists and fully blocks the airway, apnea will happen for a period of a few seconds to several minutes during sleep. It can be predicted that the tip of the epiglottis will have a maximum deformation of 1 mm, and it will not contact the back wall after the tip of the soft palate is fully collapsed. This correlates with the clinical observation that the apnea does not occur in the epiglottis region. This is due to the relatively higher stiffness of the cartilage in the epiglottis and the holding force from the surrounding tissues.

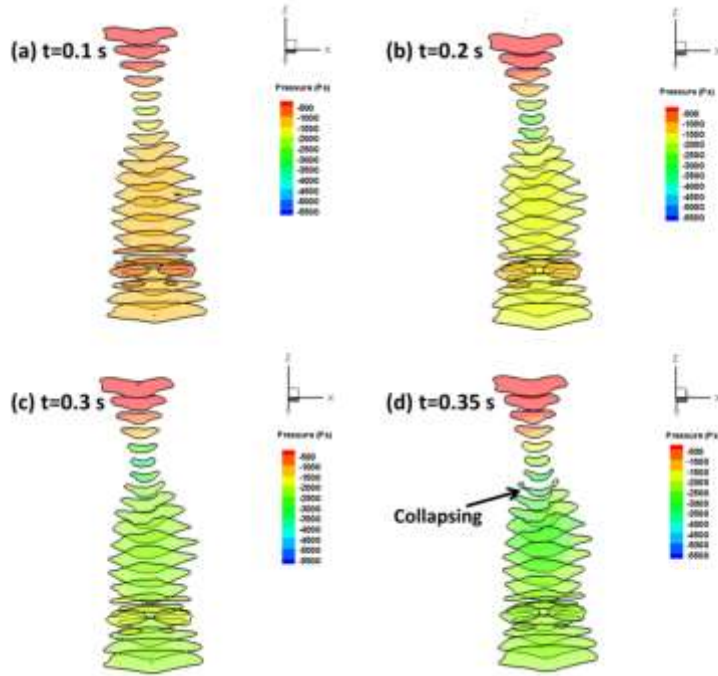


Figure 25. Pressure contour of the horizontal planes of the upper airway at time (a) 0.1 s, (b) 0.2 s, (c) 0.3 s, (d) 0.35s based on patient A.

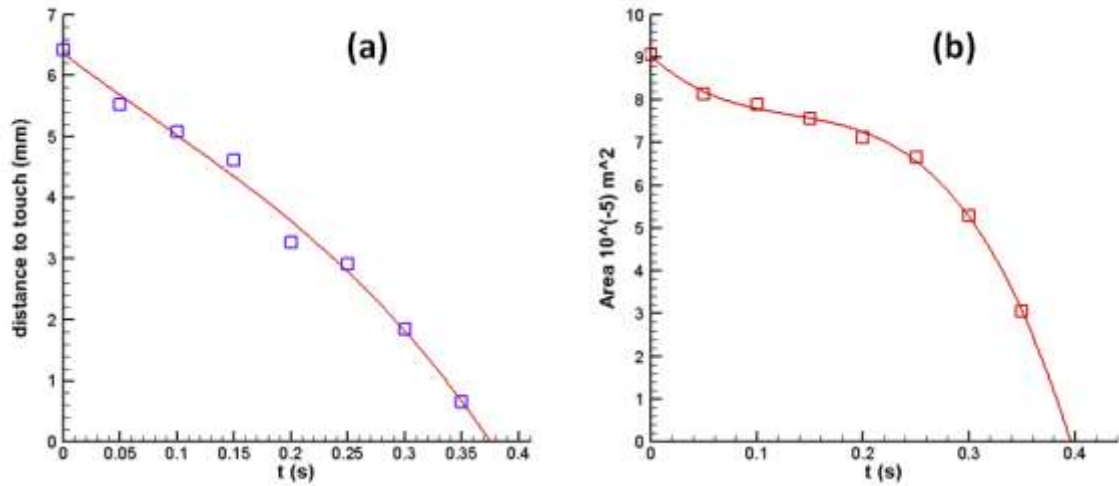


Figure 26. Prediction of (a) the first point touching and (b) full closure of the upper airway based on patient A.

5.4 Investigation of Wall Displacement

Figure 27 shows the displacement at four different parts: 1) the tip of the soft palate, 2) the base of the tongue, 3) the tip of the epiglottis, and 4) the hyoid bone based on patient A. The results indicate that the wall displacement was closely related to the fluid pressure change, as shown in Figure 27. The tip of the soft palate has experienced the largest displacement among the tissues over time, as the soft palate was predicted to collapse at first. The base of the tongue also moved back when the pressure in the oropharynx reduced. Furthermore, it can be found that the epiglottis displacement was less than that of the soft palate and the base of the tongue, which is only about 1 mm. This is due to the stiffness of the cartilage and the holding force from the surrounding tissues. The maximum deformation vector obtained from the simulation occurred at $x=2.38$ mm, $y=7.18$ mm, $z=2.78$ mm with the magnitude of 8.06 mm at the time of 0.35 s, which is observed at the tip of the soft palate, as shown in Figure 28. The airway is predicted to be fully collapsed as the intrathoracic pressure drops to -1370 Pa at 0.4 s.

It should be pointed out that the collapsible region correlates reasonably well with the published results [42, 43]. The Reynolds number of 2357 used in this study is also close to the one of 2900 studied by Zhao et al. [42, 43]. Also, Zhao et al. only used a 2 mm homogeneous thin layer tissue in their study, which means their results are less accurate and patient specific, compared to the obtained results from the present two-way FSI coupling simulation. Moreover, the intrathoracic pressure of -1370 Pa used in the present numerical simulation is the same order of magnitude as reported by Guilleminault et al. [25, 26]. These medical testing results show that the collapse of the UA typically occurs when the intrathoracic pressure falls between -20 to -40 cmH₂O,

which is equivalent to -1961.3 to $-3922.6 Pa$. The difference could be caused by the subjects' clinical characteristics.

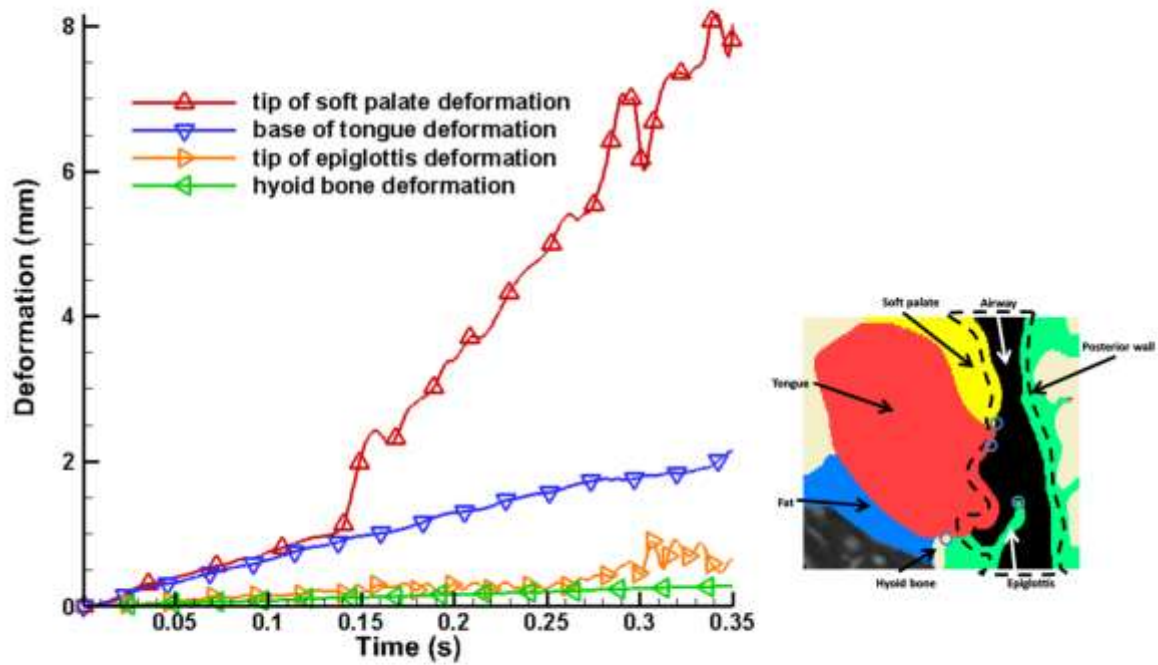


Figure 27. Deformation at four locations: the tip of the soft palate, base of the tongue, tip of the epiglottis, and hyoid bone based on patient A.

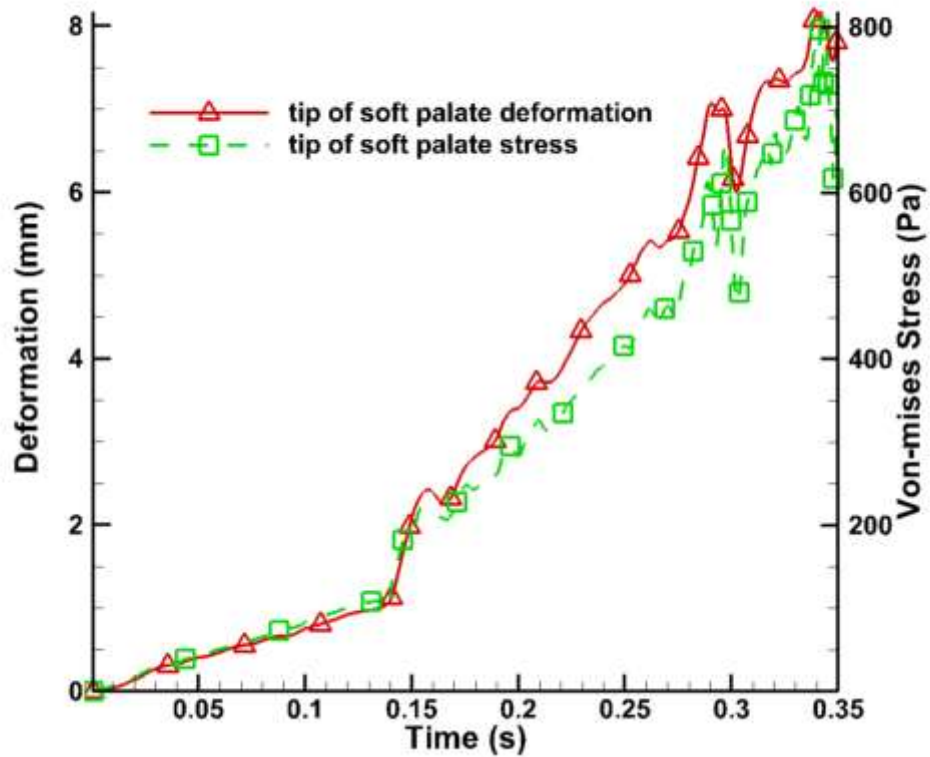


Figure 28. Deformation and stress vs. time at the tip of the soft palate based on patient A.

5.5 Conclusion

In this chapter, the patient-specific 3-D two-way FSI coupling simulation of OSA patient A's UA was developed from the CT images to study the fluid flow and soft tissue deformation during the partial breathing cycle. As the intrathoracic pressure decreased to -1370 Pa, the tip of the soft palate first reached the side wall and subsequently induced total blockage of the UA. The pressure distribution, velocity streamlines, and accurate location of the collapse region are computed and found to provide excellent first-hand clinical surgery support. This improved two-

way FSI coupling study surmounts the previously published work, which only used a homogeneous layer of tissue surrounding the UA. The present simulation starts a new approach in studying OSA by modeling the different parts along the airway.

CHAPTER 6 ASSESSMENT OF POSSIBLE TREATMENTS: SUTURE-PATCH DEVICE

6.1 Description of the Device and Material Selection

Using sutures for tongue suspension surgery has been proposed for decades, but the outcome varied from different statistical surveys [71, 72]. The stress in the suture highly depends on how the surgeon tightens it, and it is uncertain whether or not the suture will cut through tissues. Inspired by tongue piercing, medical doctors burgeoned out the idea of adding a suture-patch device, which can control not only the magnitude of the force on the suture, but also the time to apply the force. Since the main purpose is to pull the tongue forward, the study case of patient B is used in the assessment to provide a possible healing result.

The suture-patch device is intended to exert force to the base of the tongue with a suture and a patch on patient B, as shown in Figure 29. The suture goes from the epidermis to the fat under the tongue, through the digastric muscle, through the tongue from the middle where there is an approximately 2 mm wide hollow, and ends with a patch. Since the procedure is similar to tongue piercing, it may not cause too much discomfort during the healing process. The patch can be pasted on the surface of the tongue, or it can be worn with a little suction force that can hold it to the tongue. The purpose of using a patch is to let the force evenly apply on the tongue and reduce possible penetration due to high normal stress.

Medical doctors have suggested the diameter of the patch to be between 1 and 1.5 cm. Based on the size of the UA and the shape of the tongue in patient B, 1.33 cm is selected as the diameter of the patch. Three different locations: above the velopharynx (Patch location 1), at the velopharynx (Patch location 2), and below the velopharynx (Patch location 3) were selected to virtually apply the patch. The suture is straight from the center of the patch to the middle point right under the

lower jaw, so that the device can be easily fixed to the lower jaw. The present study focuses on the suture, patch, and force analysis, while the mechanical device will be designed by other student in future work.

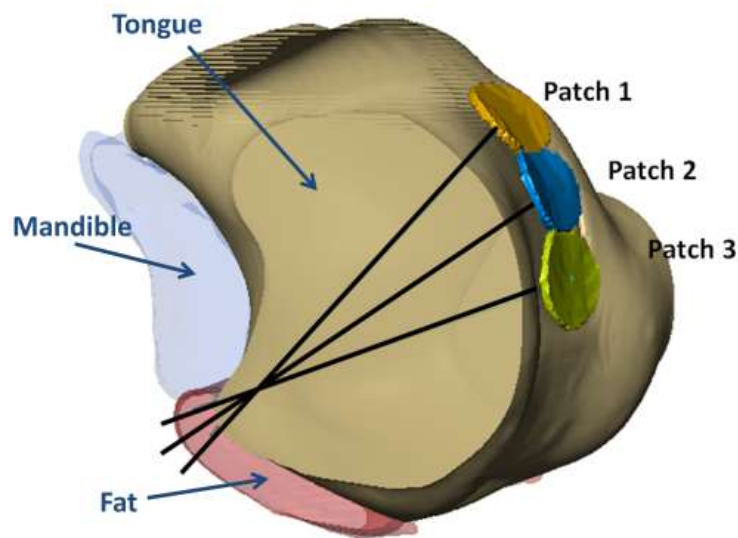


Figure 29. The suture-patch locations in the tongue on patient B.

The suture has to be non-dissolvable with low plasticity and strong thread memory (not flexible, non-braided), and works better with a round point type straight needle. The suture's surface should be smooth and even with good pliability. The suture's diameter is optimized with the diameter of 0.8 mm to prevent possible tissue cut through the tongue. Also, the suture should be pulled perpendicularly to the patch to reduce the shear stress on the tongue surface tissue. In the numerical simulation, it is assumed that the suture has very small plasticity so that it can retain

its length and strength after it is stretched. In other words, the shape change of the suture can be neglected. Then the force can be assumed to be constant through the suture.

The patch can be shaped to fit the surface of the tongue using the ScanIP software, and it then can be fabricated from a 3-D printer. The patch is designed as a round shape with the diameter of 1.33 cm and a thickness of 0.8 mm. The thickness was determined with the consideration of a computational cost in numerical simulation. However, in reality, the thickness of the patch can be 0.1~0.2 mm, as long as it is smooth with no sharp edge. The stiffness of the patch should also be considered. The patch should be light and soft; when people swallow or talk, it should move with the tongue without causing an uncomfortable foreign matter feeling for the patient. In addition, it has to be firm because it is placed to exert the force evenly on the base of the tongue in order to pull the tongue forward. The material of the plate is critical. Medical grade of titanium is chosen in the present study due to its high strength-to-weight ratio and its corrosion resistance. The material of titanium is also durable and long-lasting, as well as especially non-ferromagnetic.

The linear elasticity of different tissues used in the present study was obtained from published papers and previous experiments mentioned in Chapter 3.

6.2 Velocity Streamlines with and without Force

As mentioned in the previous section, the two-way FSI system coupling simulation was performed to study the upper airway obstruction. On the fluid side, the pressure difference between the inlet and outlet was ramped up from 0 to 200 Pa. The 3-D continuity and Navier-Stokes equations and the $k-\omega$ turbulence model are solved with the SIMPLE algorithm. Figure 30 shows the velocity streamlines without and with 5 N force on the suture at patch location 2,

and the color represents the magnitude of the velocity with the same legend. It can be found that the UA collapsed at the oropharynx without applying the force of 5 N. Shortly after the air flowed into the airway from the inlet of the mouth, a small recirculation occurred because of the fluid flow area being reduced where the hard palate was close to the middle of the tongue. A stronger recirculation occurred at the cavity between the tip of the soft palate and the back wall. The disturbance around the epiglottis is less than those mentioned by the previous literature [73], because the epiglottis, in this case study, is fully contacted with the inferior wall which results in no bifurcation. This could be a patient-specific phenomenon. After the force of 5 N was added along the suture, the airway was opened up, not only in the velopharynx region, but also in the area that under the hard palate. The air flow was slower and smoother after the force of 5 N was applied along the suture.

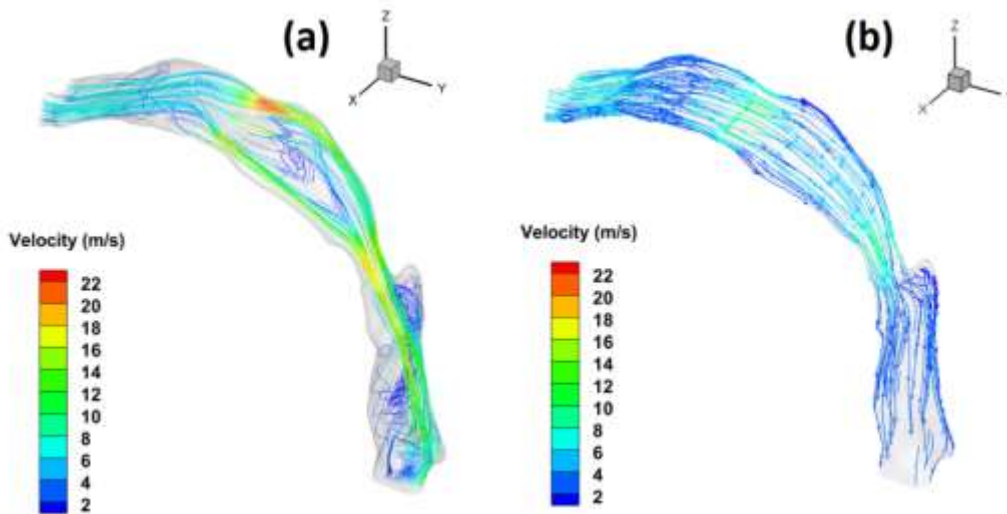


Figure 30. Velocity streamlines of the UA with (a) no force; (b) 5 N force based on patient B.

6.3 The Study of Upper Airway Collapse

The horizontal cross-sectional planes were taken at eight different locations, whose distances from the outlet are 66 mm, 62 mm, 58 mm, 54 mm, 50 mm, 46 mm, 42 mm, and 38 mm in turns, as shown in Figure 31. As shown in the figure, the upper airway collapse happened at the fourth plane where the right side of the soft palate has touched the tongue. The fifth and sixth planes also encounter the similar “touch.” At that specific moment, the volume flow rate is 0.39 L/s, and the average velocity at the velopharynx is 22.0 m/s. After the soft palate touches the base of the tongue, the reduced area will cause the pressure to drastically drop at the pharynx, which may expedite the upper airway collapse procedure.

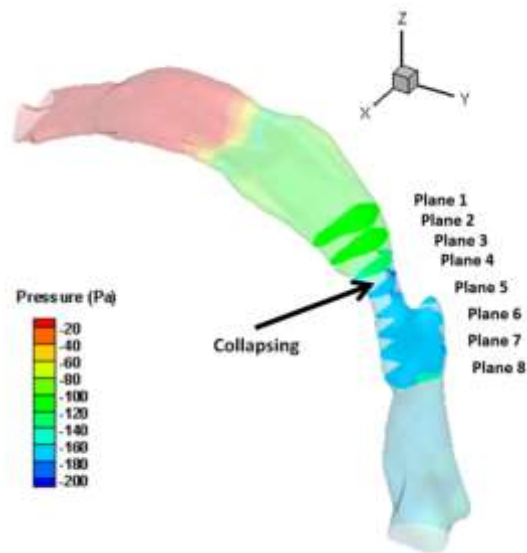


Figure 31. Cross-sectional plane showing the location of collapse based on patient B.

With the same pulling force of 5 N, the cross-sectional areas of the eight planes were calculated and compared as shown in Figure 32. Without considering the device that connected the suture to

the mandible, patches 2 and 3 can each open up plane 4 about 92% of its original area and give wider space for the air to flow through. Additionally, the increased pharyngeal area will result in a pressure rise, followed by the reduction of the soft palate deformation, and further reduces the likelihood of snoring. Patch 1 performed better in the upper area but did not perform well in the collapsing region. By contrast, both patches 2 and 3 performed well in the collapsing region. However, patch 3's vertical position might result in an uncomfortable feeling, because it is close to the epiglottis. If the applied force is released in the daytime, then the patch may slip downward along the airway and it can easily cause choking. Therefore, the location of Patch 3 is not suggested. Based on this preliminary study about this specific patient B, the location of Patch 2 is suggested, which is located right in front of the tip of the soft palate. It can open up the airway about 92% of its original area with a 5 N pulling force along the suture.

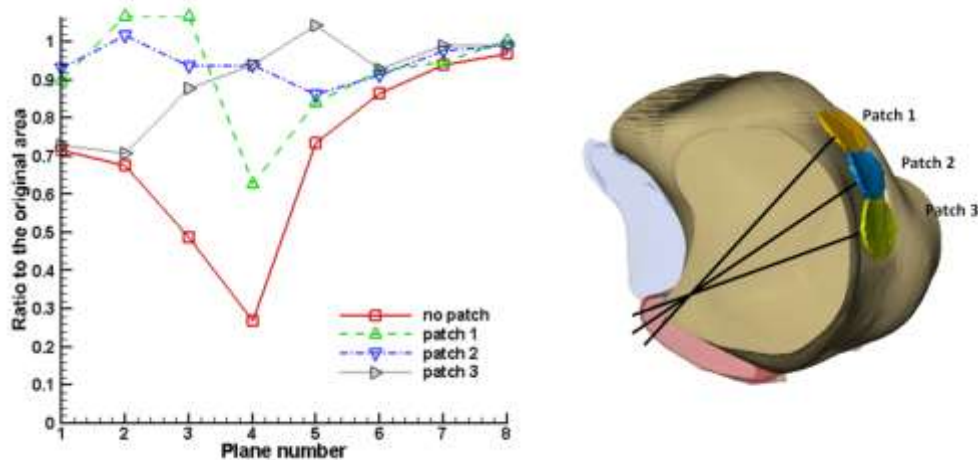


Figure 32. The area change due to the location of the patch based on patient B.

6.4 The Patch Position Study

The deformation contours with 5 N forces applied along the suture at the three patch locations during the inhaling process are shown in Figure 33. It can be found that with the applied force, the UA was opened up from collapsing. The soft palate would not collapse with the tongue after the force was applied. In fact, on each side of the tongue, there is one palatoglossal muscle connected to the soft palate that can drag the soft palate forward. However, the muscles and their interaction effects have not been considered in the present simulation due to the complication and complexity of numerical modeling. If the soft palate is dragged forward by the palatoglossal muscle, the airway from the nose will be opened up, which is also a promising result. It is noticed that the three patches are not along the same vertical line because the respiratory tract is not straight.

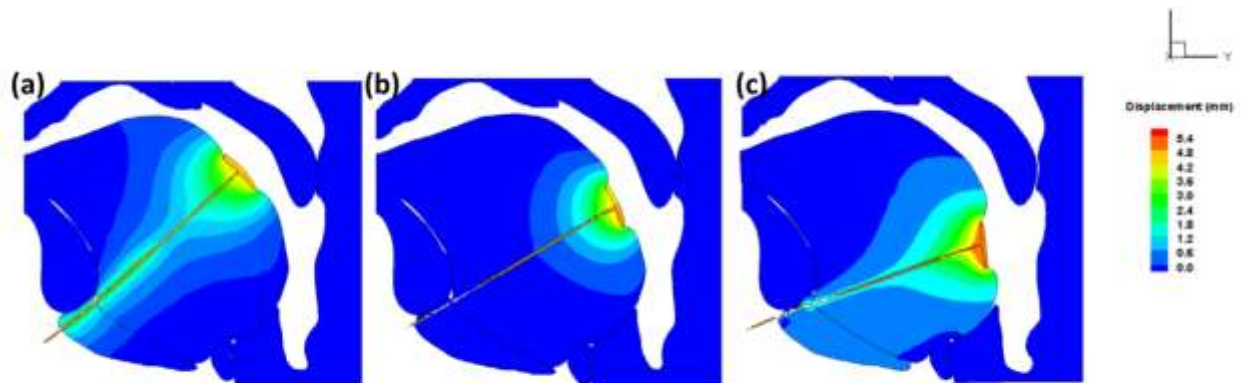


Figure 33. The deformation contour with 5 N force applied along the suture at the three patch locations based on patient B.

6.5 The von-Mises Stress

Figure 34 shows the von-Mises stress produced in the suture, patch, and tissues. As expected, variations of stress amplitudes are perceived in the suture and through the tissues. In the suture, the stress is up to 20 MPa, which results from the 5 N force on the small contact area on the tip of the suture. However, the stress on the tongue tissue is only several kPa. The area of the patch can largely reduce the normal stress on the tongue so that the equivalent stress in the tongue tissue is greatly reduced. In formerly published work, the maximum active stress values in the tongue tissues are around 150 kPa [28], but the von-Mises stress in the current study is much smaller than this “limit.”

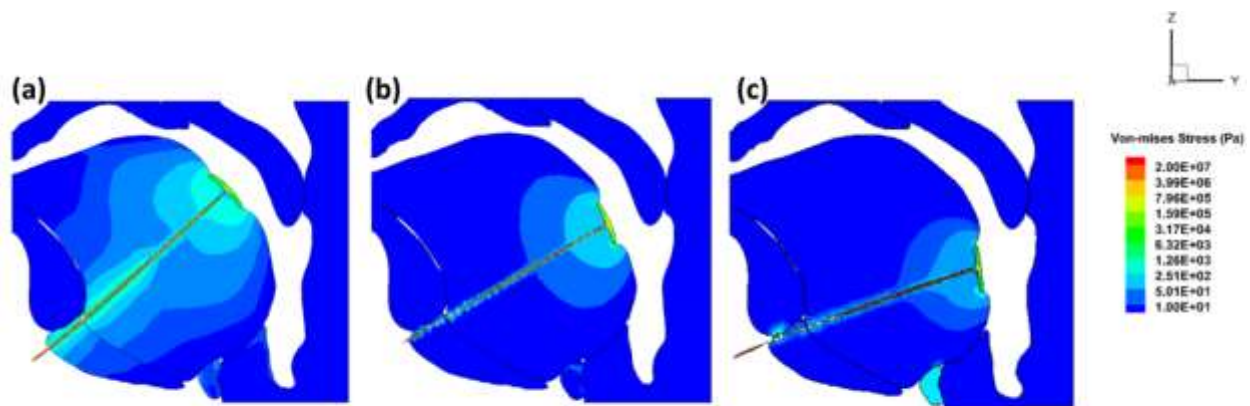


Figure 34. The von-Mises stress on the suture and in the tissue with 5 N force applied along the suture at the three patch locations based on patient B.

6.6 The Minimum Force Required

In the previous section, the initial value of 5 N is used as the pulling force. This is because the medical doctor has done clinical experiments on ramping up the pulling force on the tongues of volunteer patients and has concluded that the tongue can bear the maximum force of 22 N with a gentle drag. It is uncomfortable but the patient is still able to bear it. The patients feel more comfortable when the force is 5 N or less. Therefore, in the previous section, 5 N was used as the initial force to find the feasibility of using the suture-patch device to open up the UA. In this section, the bisection method is used to find the minimum force needed to open up the UA. The bisection method is a root-finding method that repeats bisects at an interval and selects a subinterval where the root lies for further processing. In this case, it is used to bisect the interval of effective and ineffective opening up of the UA until the minimum force able to open up the airway is found.

Prior to the bisection method, the distance between the tongue and the soft palate, where the collapse happens with no external force, is measured. Since the tip of the soft palate is where the collapse originally happened, the minimum distance should reach 0 mm when the UA is fully closed. Since both the solid and fluid mesh experience abrupt changes after the collapse of the tongue and the soft palate, the time increment needs to be extremely small, and the computational time may exceed a month to solve for the fully collapse study. The clinical experiences provided from the collaborating medical doctors have indicated that, if the minimum distance after adding the force is still below 1 mm, it can be considered as collapsing; otherwise, it is not collapsing. Therefore, the cross-sectional plane 4, which is 33.5 mm down from the inlet, is selected to study for the minimum force that can prevent the UA from collapsing.

Firstly, 2.5 N was applied along the suture as shown in Figure 35 (a). It can be seen that with 2.5 N, the patch was still able to pull the tongue away from the soft palate. The distance between the tongue and the soft palate on the left and right side were measured as 1.68 mm and 1.18 mm, respectively. Based on the collaborating medical doctor's suggestions, 2.5 N is able to open up the UA for the patient B.

For the next step, the interval between 0 N and 2.5 N was bisected, and the mean value of 1.25 N was used as the applied force. The deformation contour is shown in Figure 35 (b). The distance between the tongue and the soft palate on the left and right side were 1.60 mm and 1.13 mm, respectively. This means that 1.25 N is still able to open up the UA for patient B.

Next, the interval between 0 N and 1.25 N was bisected, and the mean value of 0.63 N was used as the applied force. The deformation contour is shown in Figure 35 (c). The distance between the tongue and the soft palate on the left and right side were 0.51 mm and 0.12 mm, respectively. This means that 0.63 N is not able to open up the UA for patient B.

Then the interval between 0.63 N and 1.25 N was bisected, and the mean value of 0.94 N was used as the applied force. The deformation contour is shown in Figure 35 (d). The distance between the tongue and the soft palate on the left and right side were 0.86 mm and 0.84 mm, respectively. This means that 0.94 N is less than the required force to open up the UA for patient B.

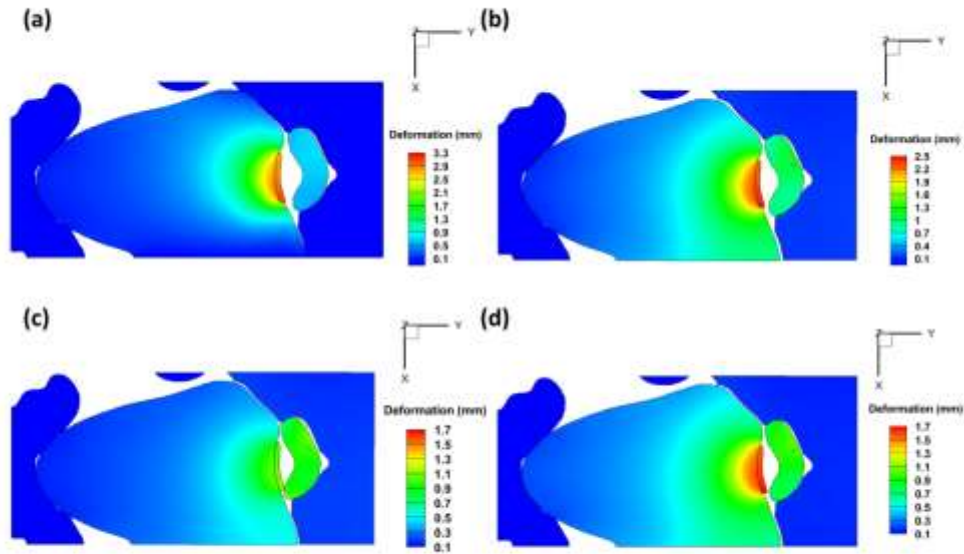


Figure 35. Top view of the cross-sectional deformation contour of plane 4 as (a) 2.5 N (b) 1.25 N (c) 0.63 N (d) 0.94 N force applied along the suture.

The bisection stops when the interval is small enough, because a human being may not feel the difference of 1.25 N and 0.94 N force with the tongue. Then the higher cap is taken into consideration, and it is suggested that the force with the magnitude of 1.25 N is sufficient to open up the UA.

The reason why the current results did not show the full collapse is that the contact between the tongue and the soft palate resulted in negative volume in the fluid domain during simulation, which stopped the two-way system coupling. Thus, in the current study, the polynomial curve fitting, as mentioned in Chapter 5, was used to predict the condition of the fully collapse. The

comparison of cross-sectional areas at selected planes with different forces applied along the suture was obtained, as shown in Figure 36. It can be seen that when the pulling force is 0, the area of plane 4 is also 0, which means full collapse started from plane 4. Plane 4, which is located at the velopharynx, is the area most prone to collapse. This result is in good agreement with the previously published results by Zhao et al. [44] and Wang et al. [41]. It can be seen that the cross-sectional area varies widely on planes 3, 4, and 5 when the different pulling forces are applied. This is because the center of the patch is on plane 4, so that the effect of the pulling force is reasonably shown on planes 3, 4, and 5.

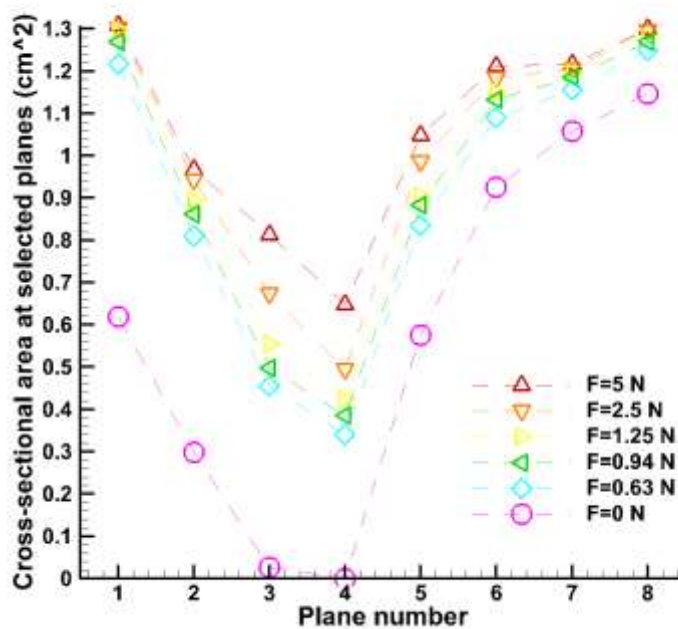


Figure 36. The cross-sectional area of plane 4 as 0-5 N forces applied along the suture.

The cross-sectional area has also been compared with the original area of the CT scan, as shown in Figure 37. It shows that when the pulling force is 0.63 N, the cross-sectional area is smaller than the original one. This can be explained by the fact that the force from the fluid flow is stronger than the pulling force from the suture to the patch. The force of 0.94 N is able to balance with the force induced by fluid flow and the force of 1.25 N is sufficient to open up the upper airway.

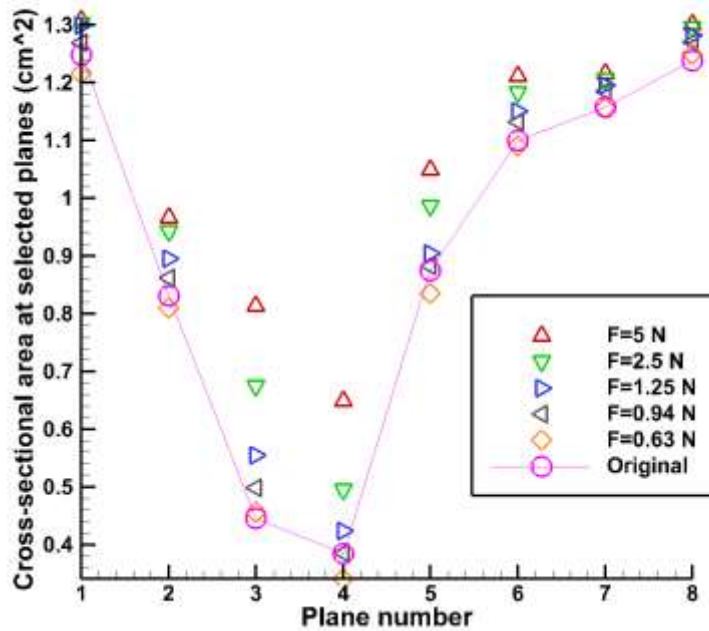


Figure 37. The cross-sectional area of plane 4 as 0.63-5 N force applied along the suture compared with the original area in the CT scan.

The collapse pressure in patient B is one order of magnitude lower than patient A, which indicates that the pressure difference varies from person to person, as mentioned by Cheng et al. [35]. However, the location of where the collapse may occur is in good agreement between the two presently studied patients and several published FSI system coupling results [40-42, 44].

6.7 Conclusion

In this present study, the suture-patch device to relieve the sleep apnea symptoms on patient B was presented and analyzed. The patch can be fabricated by a 3-D printer to better match the person's tongue shape, and the suture can be easily acquired from a hospital or medical supplier. The force can be controlled with a spring control device screwed on the lower jaw, which will be designed by another student in future work. The results show that with 5 N pulling force, the suture-patch device could open up the UA for this specific patient B. Three patch locations and the corresponding suture positions were studied, and the best of them could open up the UA 92% of its original area. The stress on the surface of the tongue was simulated and it showed using the patch can largely reduce the equivalent stress in the tissues. The bisection method has been used to find the minimum force of 1.25 N to open up the UA. Since every patient has a unique breathing habit and UA geometry, an individual patient-specific two-way FSI coupling simulation study is highly recommended when a suture-patch device is considered to be a possible treatment.

CHAPTER 7 COMPARISON OF A MALE AND A FEMALE PATIENT

7.1 Geometry Difference between the Male and the Female Patient

In this study, a male patient and a female patient were compared in terms of the geometry, fluid patterns, and tissue movement to identify common and inconsistent features. The male patient is 58-year-old with an AHI of 47/hr. The female patient is 64-year-old with an AHI of 87.6/hr. The AHI values show that the female patient has a more severe OSA. The CT scan images were imported into the ScanIP software and the medical image processing was carried out using the same procedures as mentioned in Chapter 3. From the reconstructed CT images, it can be seen that the male patient has a larger size of oropharynx compared to the female patient. The distance from the tip of the soft palate to the hyoid bone, which is the length of the oropharynx, was measured. The male's oropharynx length is about 7.28 cm and the female's is 3.68 cm. Moreover, the width/height ratio of the tongue was measured, and the male patient's ratio is 0.95 compared to the female's 0.79. It matches the clinical observation of that the male patient always has the larger flatter tongue. Furthermore, male OSA patients are claimed to have a larger cross-sectional area in their UA [74]. This agrees with the researcher's measurements that the male and female patients' narrowest cross-sectional areas are 3.0 cm^2 and 0.9 cm^2 , respectively. Figure 38 shows the midsagittal CT images of the male and female patients, and their fluid domains are shown on the right hand side.

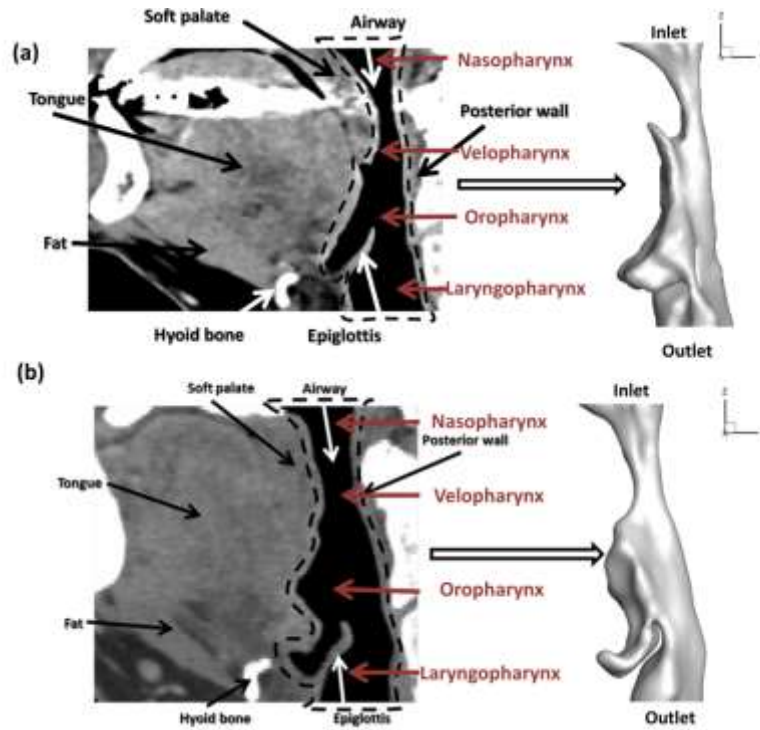


Figure 38. Respiratory- fluid domains of the male (a) and female (b) patient.

7.2 Boundary Conditions and Solver Settings

In the two-way FSI coupling simulation, the breathing pattern was modeled as a sinusoidal airflow with a peak volume flow rate of 25 L/min (average volume flow rate of 8 L/min), and within the period of 3.3 s [44]. By defining the flow rate, the researchers aimed to perceive the different behaviors of the two patients under the same breathing flow rate. A gauge pressure of 0 Pa was set at the inlet with an adjustment to the nasal cavity effect. The hydraulic diameters of 3.43 cm and 1.87 cm for the male and female patients, respectively, were used for the numerical simulation. The turbulence intensities of 6.8% and 6.7% were calculated from the Reynolds numbers 860 and 1036, based on the male and female patients, respectively. The smoothing and remeshing methods were used to adjust the moving meshes during the dynamic simulation. The

coupling between the pressure and the velocity field is implemented through the SIMPLE algorithm. On the structure side, the spine, hyoid bone, and mandible were set as the fixed supports. The top and bottom of the tissues are fixed in the z-direction, which is able to move horizontally. The contact between the tongue, soft palate, and pharyngeal walls are set as frictionless contact, while other tissues are bonded to the adjacent bone or tissue.

The density and elastic properties of the soft tissues and the bones are the same as those mentioned in Chapter 4. The difference in tissue stiffness between the male and the female patient was not considered in this comparison. The ANSYS[®] workbench 17.2 is the platform used to conduct the two-way FSI system coupling. The studied model was run on the 22-core Dell[®] PowerEdge T630 Tower Server with 128 GB memory. The calculation took about four days for each case. A uniform time increment of 0.001 s is applied during the simulation, which can provide accurate FSI results within the reasonable computing time [68].

7.3 Investigation of the Flow Field and Tissue Movement

7.3.1 Comparison of the fluid flow field

Though it was found that the male patient has a longer and flatter respiratory tract, it is not direct evidence to support the severity level of OSA. Thus, without considering the tissue stiffness and the nerve sensitivity, two-way FSI coupling simulation is used to compare the two patients' performance under the same breathing pattern and strives to find any common or inconsistent features between the two patients.

Both the male and the female patients' respiratory tracts were equally separated into 11 sections and the pressure contours of the two patients are shown in Figures 39 and 40. Both the male and female patients have negative pressure over the whole fluid domain during the inhaling process.

The negative pressure pulled the tissues together towards the UA collapse. The lowest pressure showed at the velopharynx next to the tip of the soft palate (the 4th plane for both cases). The female patient showed a lower pressure while inhaling because of her smaller sized respiratory tract. The pressure was all positive during the exhaling process, which is in good agreement with clinical observation that the UA is expanding during exhaling. The area-weighted average of pressure along the UA at the moment of peak flow rate during inhaling ($t=0.83$ s) and exhaling ($t=2.48$ s) are shown in Figure 41. The two patients' averaged pressures along the UA have the same trend. However, the female patient has a wider range of pressure change. This is caused by her smaller sized respiratory tract.

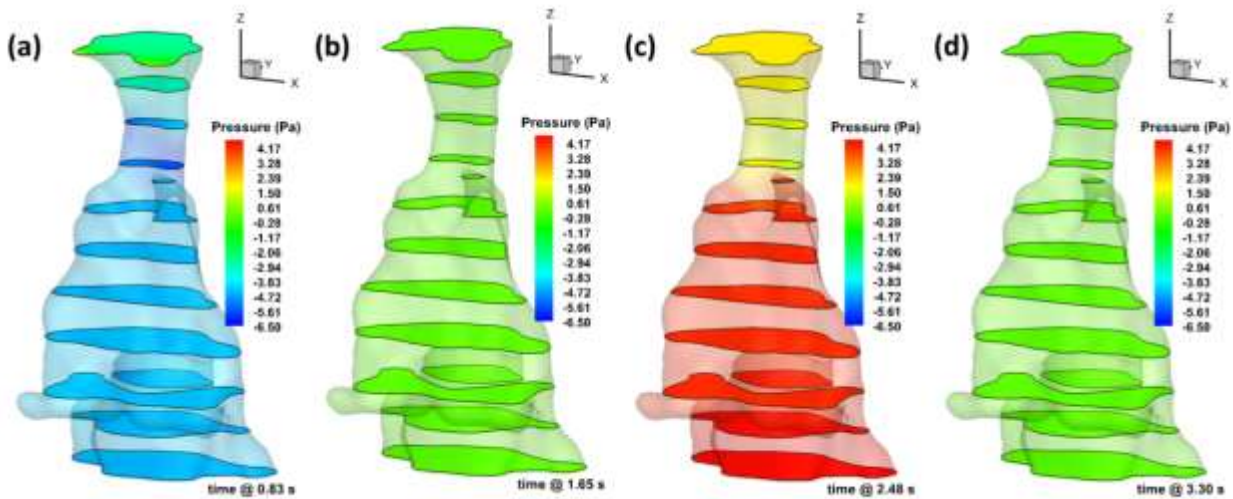


Figure 39. Pressure contour at different time for the male patient.

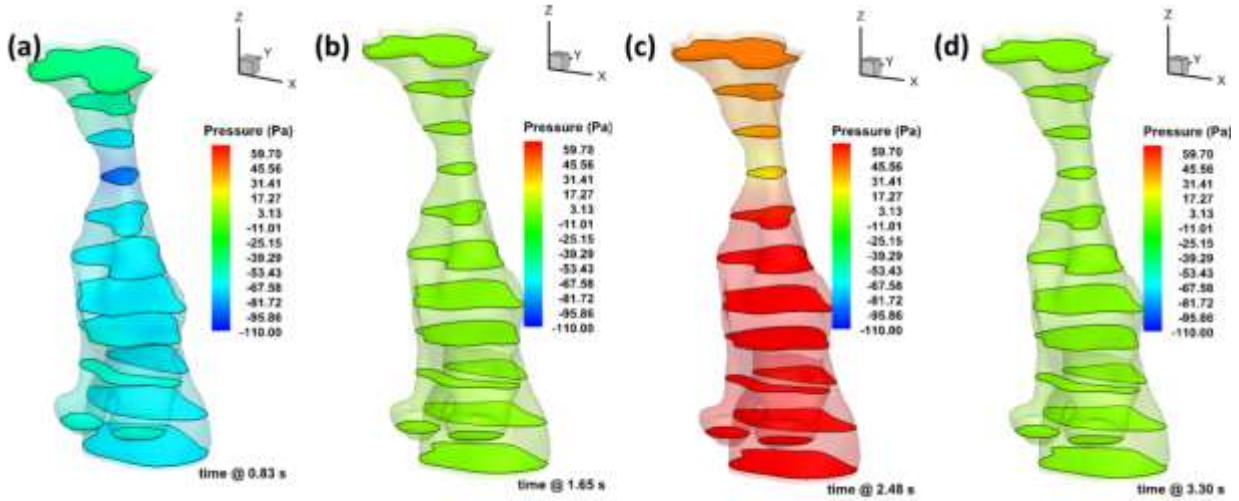


Figure 40. Pressure contour at different time for the female patient.

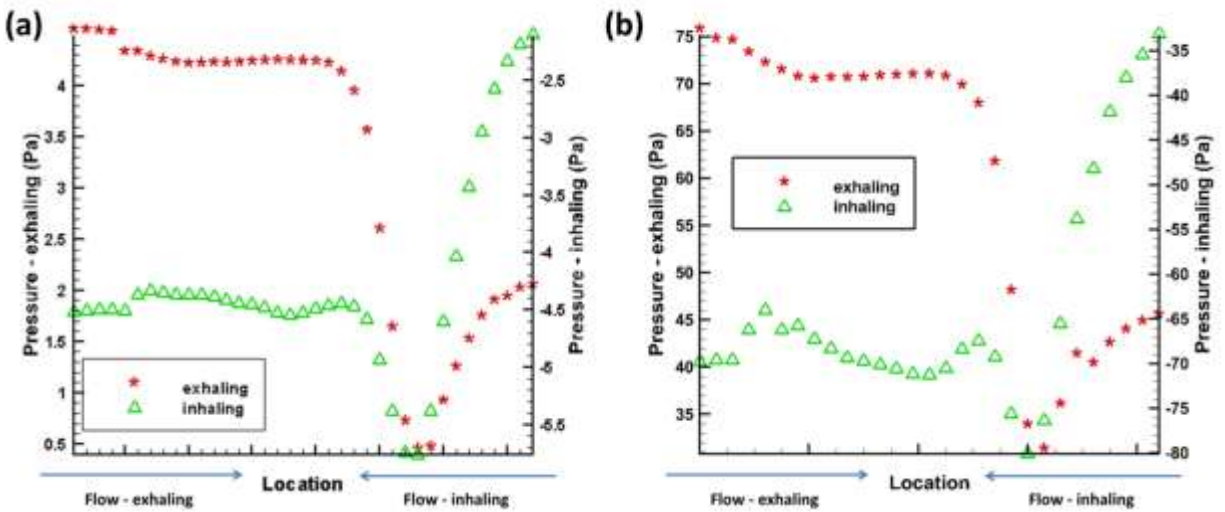


Figure 41. Area-weighted average of pressure along the upper airway at the peak flow rate

(a) the male patient (b) the female patient

Figures 42 and 43 show the streamlines at the peak inhale and exhale air flow rate in between the two zero flow rate situations. The velocity streamlines showed the female patient had a higher air flow velocity than the male patient, which is because the same flow rate was used for the two patients. The male patient has a wider area of recirculation at the oropharynx, especially behind the tongue. However, the average velocity of the recirculating fluid is smaller than that of the female patient. It is also observed that there was reverse flow on the nasopharynx side for both patients at the peak exhaling flow rate. This was caused by the adverse pressure gradient between the velopharynx and the nasopharynx during the exhaling process. It led to the reduction of the momentum of fluid flow, and thus the air flow was decelerated. Flow became nearly stagnant and the velocity was reversed, driven by the pressure difference.

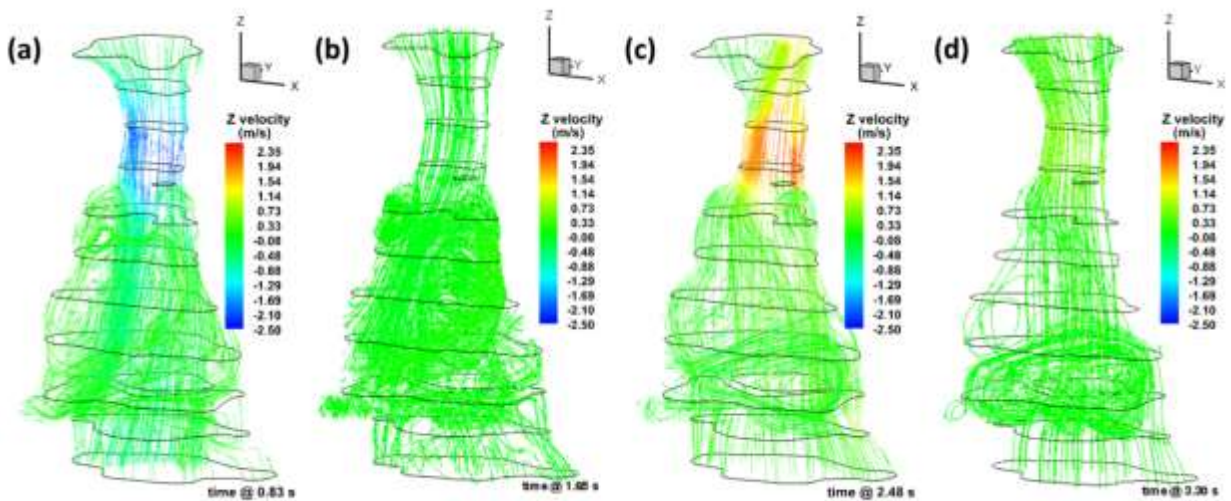


Figure 42. Velocity streamlines at different time for the male patient.

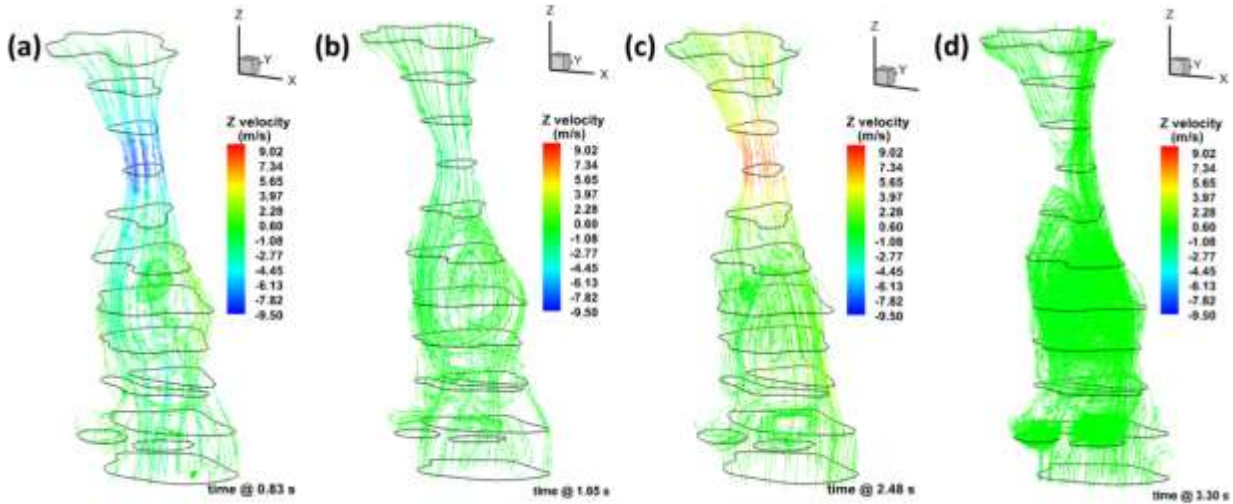


Figure 43. Velocity streamlines at different time for the female patient.

7.3.2 Comparison of the soft palate movement

Figure 44 shows the soft palate movement of the male patient in the y-direction. Regular oscillation was observed during the exhaling process. The Fast Fourier Transform (FFT) showed that the oscillation occurred with the frequency of 8.8 Hz. This frequency is about half of the one mentioned in Pirnar's paper [44]. However, the oscillation that showed when exhaling instead of inhaling is in reasonable agreement with that paper. The direction of the soft palate movement was the same as in Pirnar's paper after the inlet pressure was adjusted. The adjustment is to add pressure loss in the nasal cavity, which is not included in the present simulation.

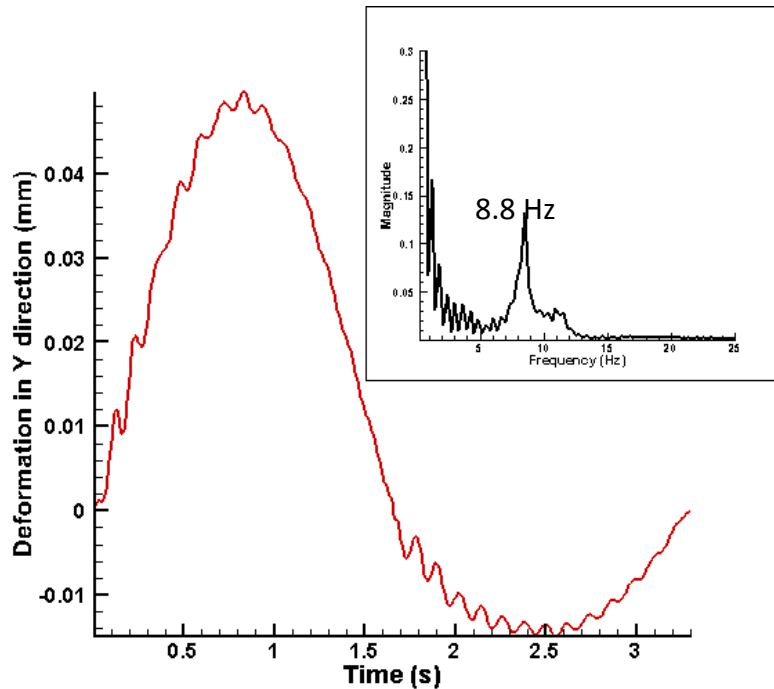


Figure 44. Tip of the soft palate movement at different time for the male patient.

Figure 45 shows the soft palate movement of the female patient. The soft palate deformation was about three times higher than that of the male patient, which is caused by the higher magnitude of the pressure in the female patient's upper airway. There is no frequency that stands out from the rest in the magnitude figure, which means the female's soft palate did not experience a regular vibration. It means that the soft palate would directly fall back until the UA is fully collapsed. It is obvious to find that the male patient has stronger soft palate vibration than the female patient. This appears in contrast with the AHI test. Normally, the severe OSA patient has the stronger vibration symptoms of the soft palate. The obtained simulation results from this study may change the way of the first judgment of the OSA, based on the patient or their

relative's observation about the classical symptoms like snoring. Patients with less snoring, or even no snoring, may have more severe OSA.

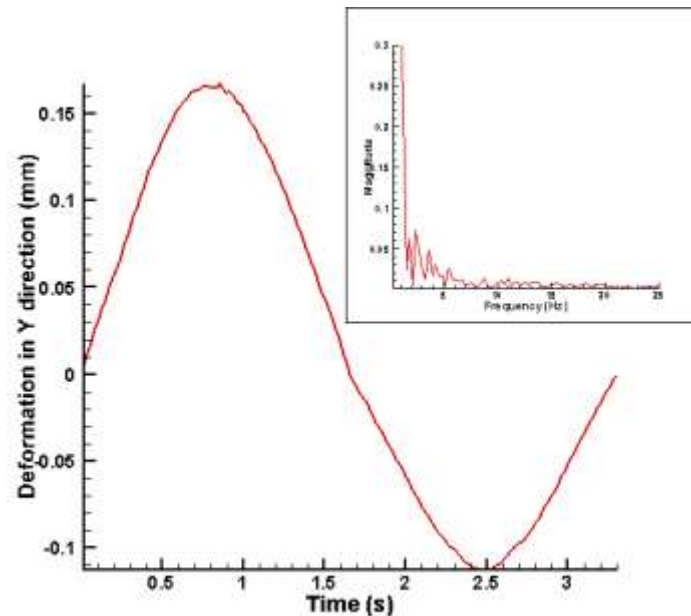


Figure 45. Tip of the soft palate movement at different time for the female patient.

7.4 Conclusion

This is a pilot study to compare one male and one female patient, both with severe OSA. Their geometry characteristics are in good agreement with the clinical observations. Their flow pattern and tissue movements have been studied and show that although the female patient has more severe OSA indicated by a higher AHI value, the male patient is more prone to show the classical symptoms like snoring. One male and one female patient do not constitute a statistically representative sample of the population. More case studies are needed to support the medical

hypothesis that women might show less classical symptoms and are underdiagnosed with OSA [75]. However, this case study shows although the female patient did not show the classic symptom of snoring, she might be diagnosed with sleep apnea or even severe sleep apnea.

CHAPTER 8 CONCLUSIONS AND FUTURE WORKS

8.1 Conclusions

OSA is a breathing disorder that causes direct and indirect symptoms in millions of patients. Fine medical CT data from two female patients and one male patient with severe OSA were obtained from the collaborating medical doctor and used in the present study. 3-D geometries were built from the CT scans using Simpleware ScanIP. The segmentation was made based on the medical image threshold and clinical experiences. The physical properties of important tissues in the UA were obtained from tests with porcine heads, and the results matched with published data, which are in good agreement with clinical consensus. The testing method could be further used *in-vivo* to test the patient-specific elasticity in live persons with slight epidermis damage, especially for those who are not able to take MREs.

A new way of solving the UA occlusion using two-way FSI coupling numerical simulation was studied. It was observed in patient A that the soft palate fell back and reached the back wall as the intrathoracic pressure went down to -1370 Pa. A further complete collapse, when the cross-sectional area reaches 0, was predicted by the curve fitting. The pressure, velocity streamlines, wall shear stress, and displacement at different locations were studied and compared. The upper airway collapse location, shown from the system coupling, agrees well with previously published works. The study provides excellent first-hand clinical surgery support. Also, the present two-way FSI coupling simulation is the first one to include all the UA surrounding tissues with different properties.

Additionally, a two-way FSI coupling numerical simulation was used to assess the outcome of surgery in patient B, placing a suture-patch device to exert force on the tongue. A novel suture-

patch was introduced and investigated virtually. The patch is shaped and sized based on the shape of the tongue. Three locations of patch placements were studied. The force of 5 N applied along the suture with patch location 2 was found to efficiently prevent airway collapse in patient B. Since the 5 N force was the initial value based on the clinical experiments, the bisection method was then used to strive for the minimum force needed. The results showed that the minimum force of 1.25 N needed to be exerted on the suture to prevent the tongue and the soft palate from collapsing, for the specific patient.

Further, air flow fields and tissue movement studies for one male patient and one female patient were compared under the same breathing rate. The male patient has a larger and flatter UA geometrically, and has a larger recirculation area in the fluid field. Moreover, the male patient has a stronger soft palate vibration than the female patient. This seems contrary to the fact that the female patient has been diagnosed with the higher AHI value. This case study shows that although the female patient did not exhibit a classic symptom like snoring, she may have serious sleep apnea syndrome.

This present work provides a pathway for developing possible medical treatments in the future. Also, the correct numerical simulation results can help medical doctors and patients to visualize the virtual results of different treatments.

8.2 Future Research

Only three severe OSA patients were studied in the present work. To test the statistical success of surgery, or to support the hypothesis using the numerical simulation study, more OSA patients with mild, medium, and severe OSA need to be studied.

Additionally, 3-D custom molded soft tissues can be used to test the experimental feasibility of the suture-patch device in future work. After the suture-patch device is successfully implemented on 3-D custom molded soft tissues, it can then be tested on English bulldogs reported with severe OSA. Finally, it can be tested on volunteer patients, and the previously mentioned personal-specific two-way FSI coupling numerical simulation can be used to predict results and optimize individual designs.

Moreover, the human body is very complicated with different muscles and nerves, as is the pharynx. In the present study, the muscles and their interaction effects are excluded from the numerical simulation because of the complication and complexity of numerical modeling. Adding the human muscles and nerves into the numerical simulation will certainly make the results more realistic and reliable, and will be a highly desired topic for the study of OSA in the future.

REFERENCES

- [1] Canto Gde, L., Pachêco-Pereira, C., Aydinoz, S., Major, P.W., Flores-Mir, C., Gozal, D. (2014). Biomarkers associated with obstructive sleep apnea: a scoping review. *Sleep Med. Rev.* 23, 28-45. <http://dx.doi.org/10.1016/j.smr.2014.11.004>.
- [2] Dickens, C. (1837). *The posthumous papers of the Pickwick club, containing a faithful record of the perambulations, perils, travels, adventures and sporting transactions of the corresponding members.* England. Chapman and hall.
- [3] Abtahi, S., Phuone, A., Major, P.W., Flores-Mir, C. (2018). Cranial base length in pediatric populations with sleep disordered breathing: A systematic review. *Sleep Med. Rev.* 39, 164-173. <https://doi.org/10.1016/j.smr.2017.09.002>
- [4] Sullivan, C.E., Jones, M.B., Issa, F.G., Eves, L. (1981). Reversal of obstructive sleep apnea by continuous positive airway pressure applied through the nares. *The Lancet*, 317(8225), 862-865. [10.1016/S0140-6736\(81\)92140-1](https://doi.org/10.1016/S0140-6736(81)92140-1)
- [5] Sullivan, C.E., Lynch, C. (1993). *US Patent No. US5245995A.* Sidney, Australia. USA Patent Office.
- [6] <https://learn.canvas.net/courses/1344/pages/anatomy-and-physiology-of-the-respiratory-system>
- [7] https://commons.wikimedia.org/wiki/File:2305_Divisions_of_the_Pharynx.jpg
- [8] <http://muscular-system.blogspot.com/2012/05/muscles-of-pharynx.html#!/2012/05/muscles-of-pharynx.html>

- [9] Vinha, P.P., Verissimo de Mello-Filho, F. (2017). Evidence of a preventive effect of breastfeeding on obstructive sleep apnea in children and adults. *J. Hum. Lact.* 33(2), 448-453. 10.1177/0890334416682006
- [10] <https://www.verywell.com/are-severe-sleep-apnea-and-cpap-pressure-correlated-3015267>
- [11] <http://www.fleetowner.com/driver-management-resource-center/how-fix-common-cpap-problems>
- [12] Wolkove, N., Baltzan, M., Kamel, H., Dabrusin, R., Palayew, M. (2008). Long-term compliance with continuous positive airway pressure in patients with obstructive sleep apnea. *Journal of the Canadian Thoracic Society*, 15(7), 365-369.
- [13] Hoffstein, V. (2007). Review of oral appliances for treatment of sleep-disordered breathing. *Sleep and Breathing*, 11(1), 1-22. 10.1007/s11325-006-0084-8.
- [14] Ruhle, K.H., Franke, K.J., Domanski, U., Nilius, G. (2011). Quality of life, compliance, sleep and nasopharyngeal side effects during CPAP therapy with and without controlled heated humidification. *Sleep and Breathing*, 15(3), 479-485. 10.1007/s11325-010-0363-2.
- [15] Gotsopoulos, H., Chen, C., Quan, J., Cistulli, P.A. (2002). Oral appliance therapy improves symptoms in obstructive sleep apnea a randomized, controlled trial. *American Journal of Respiratory and Critical Care Medicine*, 166(5), 743-748. 10.1164/rccm.200203-208OC.
- [16] <http://www.oasisdentalmilton.com/blog/sleep-apnea-appliances-offer-some-gta-patients-a-long-awaited-good-nights-rest/>
- [17] <https://doctorspiller.com/snoring-and-sleep-apnea-page-3/>

- [18] Lowe, A.A., Sjöholm, T.T., Ryan, C.F., Fleetham, J.A., Ferguson, K.A., Remmers, J.E. (2000). Treatment, airway and compliance effects of a titratable oral appliance. *Sleep*, 23(4), 172-178.
- [19] <https://www.lexingtonclinic.com/osasurgery/UPPP.html>
- [20] Sher, A.E., Schechtman, K.B., Piccirillo, J.F. (1996). The efficacy of surgical modifications of the upper airway in adults with obstructive sleep apnea syndrome. *Sleep*, 19(2),156-77.
- [21] De Luca Canto, G., Pacheco-Pereira, C., Aydinoz, S., Major, P.W., Flores-Mir, C., Gozal, D. (2015). Biomarkers associated with obstructive sleep apnea: A scoping review. *Sleep Medicine Reviews*, 23, 28-45.
- [22] Marshall, N.S., Wong, K.K.H., Cullen, S.R.J., Knuiaman, M.W., Grunstein, R.R. (2014). Sleep Apnea and 20-Year Follow-Up for All-Cause Mortality, Stroke, and Cancer Incidence and Mortality in the Busselton Health Study Cohort. *Journal of Clinical Sleep Medicine*, 10(4), 355-362. 10.5664/jcsm.3600.
- [23] Young, T., Peppard, P.E., Gottlieb, D.J. (2002). Epidemiology of Obstructive Sleep Apnea A Population Health Perspective. *American Journal of Respiratory and Critical Care Medicine*, 165(9), 1217-1239.
- [24] Sforza, E., Petiau, C., Weiss, T., Thibault, A., Krieger, J. (1999). Pharyngeal critical pressure in patients with obstructive sleep apnea syndrome. Clinical implications. *American Journal of Respiratory and Critical Care Medicine*, 159(1), 149–157. 10.1164/ajrccm.159.1.9804140.

- [25] Guilleminault, C., Chowdhuri, S. (2000). Upper airway resistance syndrome is a distinct syndrome. *American Journal of Respiratory and Critical Care Medicine*, 161,1412-1416.
- [26] Guilleminault, C., Plyares, D., Palombini, L., Koester, U., Pelin, Z., Black, J. (2001). Variability of respiratory effort in relation to sleep stages in normal controls and upper airway resistance syndrome patients, *Sleep Medicine*, 2, 397-406.
- [27] Suratt, P.M., McTier, R.F., Findley, L.J., Pohl, S.L., Wilhoit, S.C. (1987). Changes in Breathing and the Pharynx after Weight Loss in Obstructive Sleep Apnea. *Chest*, 92(4), 631-637.
- [28] Wang, Y., Liu, Y., Sun, X., Yu, S., Gao, F. (2009). Numerical analysis of respiratory flow patterns within human upper airway. *Acta Mechanica Sinica*, 25, 737-746. 10.1007/s10409-009-0283-1.
- [29] Mylavarapu, G., Murugappan, S., Mihaescu, M., Kalra, M., Khosla, S., Gutmark, E. (2009). Validation of computational fluid dynamics methodology used for human upper airway flow simulations. *Journal of Biomechanics*, 42(10),1553-1559.
- [30] Liu, Y., Ye, J., Liu, Z., Huang, L., Luo, H., Li, Y. (2012). Flow oscillation—a measure to predict the surgery outcome for obstructed sleep apnea (OSA) subject. *Journal of Biomechanics*, 45, 2284-2288.
- [31] Fletcher, A., Choi, J., Awadalla, M., Potash, A.E., Wallen, T.J., Fletcher, S., Chang, E.H. (2013). The effect of genioglossal advancement on airway flow using a computational flow dynamics model. *Laryngoscope*, 123(12),3227-3232.
- [32] Mylavarapu, G., Mihaescu, M., Fuchs, L., Papatziamos, G. (2013). Planning human upper airway surgery using computational fluid dynamics. *Journal of Biomechanics*, 46, 1979-1986.

- [33] Luo, H., Sin, S., McDonough, J.M., Isasi, C.R., Arens, R., Wootton, D.M. (2014). Computational fluid dynamics endpoints for assessment of adenotonsillectomy outcome in obese children with obstructive sleep apnea syndrome. *Journal of Biomechanics*, 47, 2498-2503.
- [34] Yu, C.C., Hsiao, H.D., Tseng, T.I., Lee, L.C., Yao, C.M., Chen, N.H., Wang, C.J., Chen, Y.R. (2012). Computational fluid dynamics study of the inspiratory upper airway and clinical severity of obstructive sleep apnea. *Journal of Craniofacial Surgery*, 23(2), 401-405.
- [35] Cheng, G.C., Koomullil, R.P., Ito, Y., Shih, A.M., Sittitavornwong, S., Waite, P.D. (2014). Assessment of surgical effects on patients with obstructive sleep apnea syndrome using computational fluid dynamics simulations. *Mathematics and Computers in Simulation*, 106, 44-59. 10.1016/j.matcom.2012.11.008.
- [36] Sun, X., Yu, C., Wan, Y., Liu, Y. (2007). Numerical simulation of soft palate movement and airflow in human upper airway by fluid-structure interaction method. *Acta Mechanica Sinica*, 23(4), 359-367. 10.1007/s10409-007-0083-4.
- [37] Chouly, F., Hirtum, A.V., Lagree, P.Y., Pelorson, X., Payan, Y. (2008). Numerical and experimental study of expiratory flow in the case of major upper airway obstructions with fluid-structure interaction. *Journal of Fluids and Structures*, 24, 250-269.
- [38] Mylavaram, G., Murugappan, S., Mihaescu, M., Kalra, M., Khosla, S., Gutmark, E. (2009). Validation of computational fluid dynamics methodology used for human upper airway flow simulations. *Journal of Biomechanics*, 42(10), 1553-1559. 10.1016/j.jbiomech.2009.03.035.

- [39] Huang, R., Rong, Q. (2010). Respiration simulation of human upper airway for analysis of obstructive sleep apnea syndrome. *Life System Modeling and Intelligent Computing*, 6330, 588-596.
- [40] Zhu, J.H., Lee, H.P., Lim, K.M. (2012). Passive movement of human soft palate during respiration: A simulation of 3D fluid structure interaction. *Journal of Biomechanics*, 45(11), 1992-2000.
- [41] Wang, Y., Wang, J., Liu, Y., Yu, S., Sun, X., Li, S., Shen, S., Zhao, W. (2012). Fluid-structure interaction modeling of upper airways before and after nasal surgery for obstructive sleep apnea. *International Journal for Numerical Method in Biomedical Engineering*, 28, 528-546.
- [42] Zhao, M., Barber, T., Cistulli, P.A., Sutherland, K., Rosengarten, G. (2013). Simulation of upper airway occlusion without and with mandibular advancement in obstructive sleep apnea using fluid-structure interaction. *Journal of Biomechanics*, 46(15), 2586-2592.
- [43] Zhao, M., Barber, T., Cistulli, P.A., Sutherland, K., Rosengarten, G. (2014). Using two-way fluid-structure interaction to study the collapse of the upper airway of OSA patients. *Applied Mechanics and Materials*, 553, 275-280.
- [44] Pirnar, J., Dolenc-Groselj, L., Fajdiga, I., Zun, I. (2015). Computational fluid-structure interaction simulation of air flow in the human upper airway. *Journal of Biomechanics*, 48, 3685-3691.
- [45] Swift, A.C., Campbell, I.T., Mckown, T.M. (1988). Oronasal obstruction, lung volumes, and arterial oxygenation. *The Lancet*, 1(8577), 73-75. 10.1016/S0140-6736(88)90282-6.

- [46] Elad, D., Wolf, M., Keck, T. (2008). Air-conditioning in the human nasal cavity. *Respiratory Physiology and Neurobiology*, 163(1-3), 121-127. 10.1016/j.resp.2008.05.002.
- [47] Kobayashi, E., Hishikawa, S., Teratani, T., Lefor, A.T. (2012). The pig as a model for translational research: overview of porcine animal models at Jichi Medical University. *Transplantation Research*, 1(8), 1-9.
- [48] <http://www.tainstruments.com/products/electroforce-mechanical-testers/>
- [49] Payan, Y., Ohayon, J. (2017). Biomechanics of living organs hyperelastic constitutive laws for finite element modeling. Cambridge, MA.: Elsevier/Joe Hayton.
- [50] Stoohs, R., Guilleminault, C. (1991). Snoring during NREM sleep: Respiratory timing, esophageal pressure and EEG arousal. *Respiration Physiology*, 85(2), 151-167. 10.1016/0034-5687(91)90058-Q.
- [51] Wang, Y., Elghobashi, S. (2014). On locating the obstruction in the upper airway via numerical simulation. *Respiratory Physiology and Neurobiology*, 193,1-10.
- [52] Chen, E.J., Novakofski, J., Jenkins, W.K., O'Brien Jr, W.D. (1996). Young's modulus measurements of soft tissues with application to elasticity imaging. *IEEE Transactions on Ultrasonics, Ferroelectrics, and Frequency Control*, 43(1), 191-194.
- [53] Cheng, S., Gandevia, S.C., Green, M., Sinkus, R., Bilston, L.E. (2011). Viscoelastic properties of the tongue and soft palate using MR elastography. *Journal of Biomechanics*, 44, 450-454. 10.1016/j.jbiomech.2010.09.027
- [54] Fung, Y.C. (1993). Biomechanics mechanical properties of living tissues. New York, NY.: Springer.

- [55] Malhotra, A., Huang, Y., Fogel, R.B., Pillar, G., Edwards, J.K., Kikinis, R., Loring, S.H., White, D.P. (2002). The male predisposition to pharyngeal collapse: importance of airway length. *American Journal of Respiratory and Critical Care Medicine*, 166(10), 1388-1395. 10.1164/rccm.2112072.
- [56] Xu, C., Brennick, M.J., Wootton, D.M. (2005). Image-based three-dimensional finite element modeling approach for upper airway mechanics. *Engineering in Medicine and Biology*, 3, 2587-2590. 10.1109/IEMBS.2005.1616998.
- [57] Payan, Y., Bettega, G., Raphael, B. (1998). A biomechanical model of the human tongue and its clinical implications. *Medical Image Computing and Computer-Assisted Intervention*, 1946, 688-695. 10.1007/BFb0056255.
- [58] Gerard, J.M., Ohayon, J., Luboz, V., Perrier, P., Payan, Y. (2005). Non-linear elastic properties of the lingual and facial tissues assessed by indentation technique: Application to the biomechanics of speech production. *Medical Engineering and Physics*, 27(10), 884-892. 10.1016/j.medengphy.2005.08.001.
- [59] Stavness, I., Lloyd, J.E., Fels, S. (2012). Automatic prediction of tongue muscle activations using a finite element model. *Journal of Biomechanics*, 45(16), 2841-2848. 10.1016/j.jbiomech.2012.08.031.
- [60] Gilbert, R.J., Napadow, V.J., Gaige, T.A., Wedeen, V.J. (2007). Anatomical basis of lingual hydrostatic deformation. *Journal of Experimental Biology*, 210(23), 4069-4082.

- [61] Yousefi, A.K., Nazari, M.A., Perrier, P., Panahi, M.S., Payan, Y. (2018). A visco-hyperelastic constitutive model and its application in bovine tongue tissue. *Journal of Biomechanics*, 71, 190-198.
- [62] Humphrey, J.D. (2003). Continuum biomechanics of soft biological tissues. *The royal society*, 459, 3-46.
- [63] Tsokos, M., Byard, R. (2012). Putrefactive “rigor mortis”. *Forensic Science, Medicine, and Pathology*, 8(2), 200-201. 10.1007/s12024-011-9232-y
- [64] Wilcox, D.C. (1988). Re-assessment of the scale-determining equation for advanced turbulence models. *AIAA Journal*, 26(11), 1299-1310.
- [65] Gupta, J.K., Lin, C.H., and Chen, Q. (2010). Characterizing exhaled airflow from breathing and talking. *Indoor Air*, 20, 31-39.
- [66] Brown, A.G., Shi, Y., Marzo, A., Staicu, C.S., Valverde, I., Beerbaum, P., Lawford, P.V., Hose, D.R. (2012). *Journal of Biomechanics*, 45(3), 516-523.
- [67] Barton, I.E. (1998). Comparison of SIMPLE- and PISO-type algorithms for transient flows. *International Journal for Numerical Methods in Fluids*, 26, 459-483. 10.1002/(SICI)1097-0363(19980228)26:4<459::AID-FLD645>3.0.CO;2-U.
- [68] Siqueira, J.C.G., Bonatto, B.D., Marti, J.R., Hollman, J.A., Dommel, H.W. (2015). A discussion about optimum time step size and maximum simulation time in EMTP-based programs. *International Journal of Electrical Power and Energy Systems*, 72, 24-32. 10.1016/j.ijepes.2015.02.007.

- [69] Liu, Y., Mitchell, J., Woosoon, Y., Chen, Y., Wang, R.C. (2014). Frequency dependent viscoelastic properties of porcine upper airway. 7th World Congress of Biomechanics, Jul, 6-11, Boston, USA.
- [70] Heenan, A.F., Matida, E., Pollard, A. (2003). Experimental measurements and computational modeling of the flow field in an idealized human oropharynx. *Experiments in Fluids*, 35(1), 70-84. 10.1007/s00348-003-0636-7.
- [71] Pang, K.P., Terris, D.J. (2006). Tongue suspension suture in obstructive sleep apnea. *Operative Techniques in Otolaryngology-Head and Neck Surgery*, 17(4), 252-256.
- [72] Woodson, B.T. (2001). A tongue suspension suture for obstructive sleep apnea and snorers. *Otolaryngology-Head and Neck Surgery*, 124, 297-303.
- [73] Liu, Y., Mitchell, J., Chen, Y., Yim, W., Chu, W., Wang, R.C. (2018). Study of the upper airway of obstructive sleep apnea patient using fluid structure interaction. *Respiratory Physiology and neurobiology*, 249, 54-61. 10.1016/j.resp.2018.01.005.
- [74] Lin, C.M., Davidson, T.M., Ancoli-Israel, S. (2008) Gender differences in obstructive sleep apnea and treatment implications. *Sleep Med Rev*, 12(6), 481-496.
- [75] Young, T., Hutton, R., Finn, L., Salfan, B., Palta, M. (1996). The gender bias in sleep apnea diagnosis. Are women missed because they have different symptoms? *Arch Intern Med*, 156 (21):2445–2451.

CURRICULUM VITAE

Graduate College

University of Nevada, Las Vegas

Yang Liu

Email address: yangliu205@gmail.com

Education

Master of Science, Mechanical Engineering, 2011

University of Nevada, Las Vegas

Bachelor of Engineering, Electrical Engineering, 2008

Harbin Institute of Technology, Harbin, China

Publications

- Li, J., Chen, Y., Liu, Y. (2011). Mathematical simulation of metamaterial solar cells. *Advances in Applied Mathematics and Mechanics*, 3(6), 702-715. 10.4208/aamm.11-m1109.

- Liu, Y., Chen, Y., Li, J., Hung, T.C., Li, J. (2012). Study of energy absorption on solar cell using metamaterials. *Solar Energy*, 86(5), 1586-1599. 10.1016/j.solener.2012.02.021.
- Liu, Y., Mitchell, J., Yim, W., Chen, Y., Wang, R.C. (2014). Frequency dependent viscoelastic properties of porcine upper airway. Poster session presented at: *7th World Congress of Biomechanics*. July 6-11; Boston, USA.
- Mitchell, J., Liu, Y., Wang, R.C., Orr, K., Yim, W., Chen, Y. (2014). A new technique of virtual modeling of individual patient airways in obstructive sleep apnea. *Otolaryngol Head Neck Surgery*, 151(1), 261-262.
- Liu, Y., Mitchell, J., Chen, Y., Yim, W., Chu, W., Wang, R.C. (2018). Study of the upper airway of obstructive sleep apnea patient using fluid structure interaction. *Respiratory Physiology and Neurobiology*, 249, 54-61. 10.1016/j.resp.2018.01.005.
- Liu, Y., Chen, Y., Yim, W., Wang, R.C. (2018) Study of the suture-patch device through the tongue for sleep apnea using fluid-structure interaction modeling. *Journal of Otolaryngology and Rhinology*, 4(48), 1-9. 10.23937/2572-4193.1510048.